Since everolimus as well as cyclosporine and tacrolimus are metabolized by cytochrome P450 (CYP) 3A and also transported via P-glycoprotein,[7-9] pharmacokinetic interactions may vary between everolimus and tacrolimus or cyclosporine.

Here, we report pharmacokinetic differences between sirolimus and everolimus in two pancreatic islet transplant patients concomitantly administered tacrolimus. The blood concentration of everolimus was measured by fluorescence polarization immunoassay (FPIA) method as well as high performance liquid chromatography with mass spectrometry (LC/MS).

Methods

Ethics: These studies were conducted in accordance with the Declaration of Helsinki and its amendments and were approved by the Kyoto University Graduate School and Faculty of Medicine Ethics Committee. Written informed consent was obtained from each patient.

Monitoring of blood concentrations for immunosuppressants: Whole blood concentrations of sirolimus (Rapamune®, Wyeth, Madison, NJ) were measured by high performance liquid chromatography with ultraviolet detection (HPLC-UV) as described previously.[10] The whole blood concentration of everolimus (Certican®, Novartis Pharma AG, Basel, Switzerland) was determined by a FPIA (Innofluor® Certican® Assay, Seradyn, Inc., Indianapolis, IN) using a TDxFLx® analyzer (Abbott Japan Co. Ltd., Tokyo, Japan).

Remnant blood samples after measurement of everolimus by FPIA were stored at −80°C. Everolimus and sirolimus whole blood concentrations were determined by a liquid-liquid extraction procedure and analysis of the extract by LC/MS in selected ion monitoring mode using atmospheric pressure chemical ionization as an interface at the laboratory of Novartis Pharma S. A. S. (Rueil Malmaison, France). Assay quantification limits were 0.3 ng/mL for everolimus and 0.5 ng/mL for sirolimus.

Cross-reactivity of sirolimus with the antibody for everolimus: To evaluate the cross-reactivity of sirolimus with the antibody for everolimus used in the assay, sirolimus was spiked in control human whole blood and sirolimus concentration was measured using FPIA for everolimus. Sirolimus concentrations were prepared at 5, 10, 20 and 50 ng/mL and tested in triplicate.

Time course study of everolimus in islet transplant patients: On the day immediately before the discharge of each patient, a time course study of everolimus was conducted. Blood samples were collected just before and 1, 2, 4, and 8 hrs after the morning administration. Whole blood concentrations of everolimus were determined using LC/MS at the laboratory of Novartis.

Results

Case report: Patient 1, a 48-year-old Japanese woman, had been treated with sirolimus and tacrolimus (Prograf®, Astellas Pharma Inc., Tokyo, Japan) after islet transplantation, according to the Edmonton protocol.[1] Thirty-six days after the transplantation, the mTOR inhibitor was converted. We called the day of conversion day 0. Both everolimus and sirolimus were administered on day 0 and only everolimus was administered after that. She kept taking tacrolimus as before (3–4 mg/day). Sirolimus was administered once a day. Everolimus and tacrolimus were administered twice daily. Blood sampling was performed once a day in the morning before the next administration of drugs. Before day 0, the whole blood concentration of sirolimus was quantified by HPLC-UV to adjust the trough concentration of sirolimus to 12–15 ng/mL. After day 0, the dosage of everolimus was adjusted to achieve a target trough blood concentration of 12–15 ng/mL as determined by FPIA. On day 0, the administration of everolimus was started at 4 mg/day, which was less than the dosage of sirolimus on day −1 (5 mg/day). Since the trough concentration of everolimus gradually decreased, the everolimus dosage was increased to 10 mg/day and the blood concentration reached the target level (**Fig. 1**, upper panel).

Patient 2, a 41-year-old Japanese woman, started the administration of everolimus 63 days after transplantation. Based on experience with patient 1, from the start, she was administered 12 mg/day of everolimus, this being greater than the dosage of sirolimus on day −1 (9 mg/day). As a result she did not experience a remarkable fall in the trough concentration of everolimus (**Fig. 1**, lower panel). During the switch from sirolimus to everolimus, she was concomitantly administered 4–6 mg/day of tacrolimus.

Neither patient showed remarkable change in tacrolimus trough concentration, which remained at 3–6 ng/mL, or had clinical complications during the study period. Neither patient was treated with potent inducers or inhibitors of CYP3A and P-glycoprotein.

Pharmacokinetic analysis: Whole blood concentrations of everolimus and sirolimus after the conversion were determined using LC/MS. After discontinuance of administration, sirolimus remained in the blood for several days (**Fig. 1**). The concentration of everolimus measured by FPIA was greater than that obtained by LC/MS, especially immediately after the conversion. To evaluate the cross-reactivity of sirolimus with the antibody for everolimus in the assay, we measured concentrations of sirolimus spiked in control human whole blood using FPIA for everolimus. As shown in **Figure 2**, the antibody for everolimus showed extensive cross-reactivity with sirolimus ([Detected as everolimus] = 1.43 + 0.47 × [Sirolimus concentration], $r^2 = 0.992$).

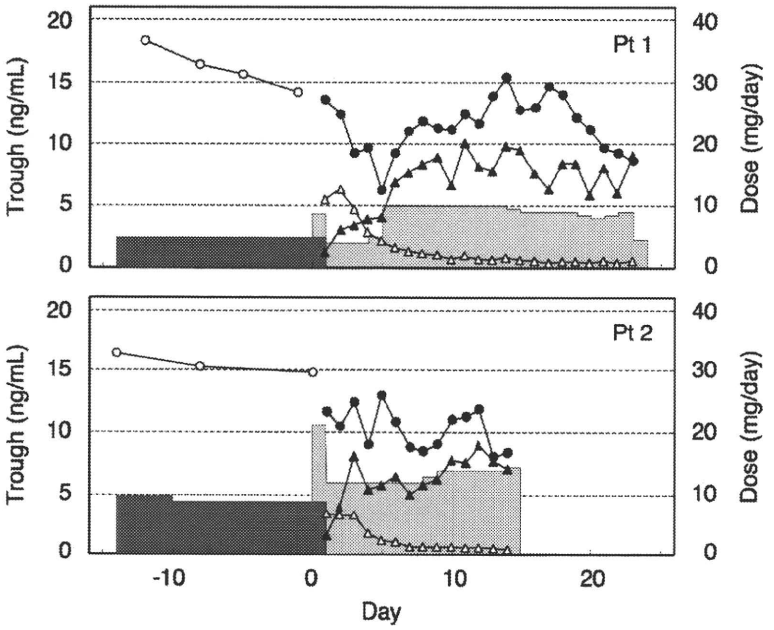

Fig. 1. Trough blood concentrations of sirolimus measured by HPLC-UV (open circles) and LC-MS (open triangles) and those of everolimus measured by FPIA (closed circles) and LC-MS (closed triangles) are plotted for each patient
Dark and light shaded areas show daily dosages of sirolimus and everolimus, respectively.

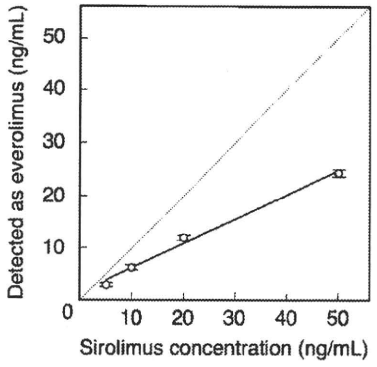

Fig. 2. Sirolimus blood concentrations measured by the FPIA method for everolimus. Each point represents the mean ± SD (n = 3)
The solid line shows the fitting line. The dotted line represents the line of identity (*i.e.*, slope = 1).

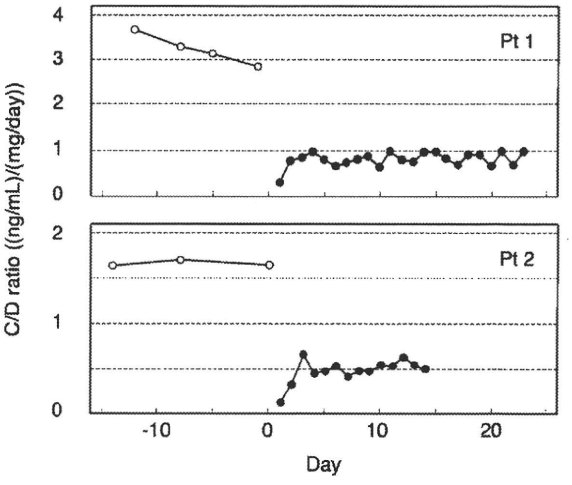

Fig. 3. The trough concentration per dose (C/D) ratios of sirolimus (open circles) and everolimus (closed circles) were plotted for each patient

Figure 3 shows the trough concentration per dose (C/D) ratio profiles of sirolimus and everolimus. C/D ratios of everolimus were calculated from concentrations determined by LC/MS and the dosage administered on the previous day. In patient 1, C/D ratios of sirolimus and everolimus were 3.26 ± 0.35 (ng/mL)/(mg/day) (mean ± standard deviation, n = 4) and 0.87 ± 0.12 (n = 22, except day 1), respectively. In patient 2, the ratios were 1.67 ± 0.03 (n = 3) and 0.52 ± 0.09 (n = 13, except day 1), respectively. In each patient, the C/D ratio of everolimus was approximately three times less that of sirolimus. C/D ratios of everolimus and sirolimus in patient 1 were twice those in patient 2.

We performed a time course study on everolimus. On day 23 for patient 1 and day 13 for patient 2. Everolimus concentration profiles measured by LC/MS are shown in **Figure 4**. Patient 1 was administered 4.5 mg everolimus and the peak concentration (17.1 ng/mL) was obtained at

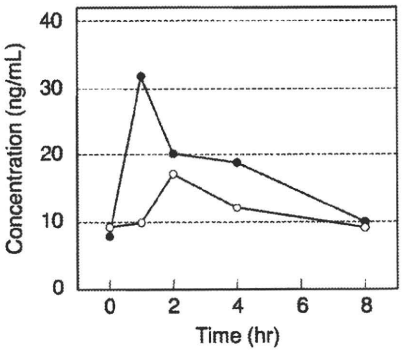

Fig. 4. Everolimus blood concentration profiles after oral administration in the two patients
Open and closed circles show everolimus concentration of patient 1 and patient 2, respectively.

2 h after the administration. Patient 2 was administered 7 mg everolimus and the peak concentration (31.8 ng/mL) was obtained at 1 h. The areas under the concentratioin-time curve from 0 to 8 h (AUC_{0-8}) calculated by the trapezoidal method were 94 and 142 ng·hr/mL in patient 1 and patient 2, respectively, while the concentrations at pre-dose and 8 h in patient 1 were nearly the same as those in patient 2, respectively.

Discussion

As shown in **Figure 1**, our patients were administered 8–14 mg/day of everolimus (with tacrolimus), and achieved trough concentrations of 5–10 ng/mL as measured by the LC/MS. Compared with other reports in which 1.5 or 3 mg/day of everolimus with cyclosporine were administered to renal transplant patients to maintain trough concentrations in a similar range,[11,12] our doses were quite large. We consider that this discrepancy mainly resulted from the difference in calcineurin inhibitor used, namely tacrolimus or cyclosporine. Everolimus as well as tacrolimus and cyclosporine are substrates of CYP3A and P-glycoprotein,[7–9] but lower blood concentrations of tacrolimus than cyclosporine in the clinical situation compared with each affinity value may have little influence on the pharmacokinetics of everolimus. Recently, Kovarik *et al.*[13] reported that the level of exposure to everolimus was 2.5 fold higher with cyclosporine than tacrolimus. It has been reported that average everolimus predose blood concentrations were significantly lower by 2.9 fold in the absence compared with the presence of cyclosporine.[12] The trough concentrations of sirolimus with cyclosporine are reported to be 1.42 times higher than those with tacrolimus.[14] Taking these findings into consideration, cyclosporine has a more profound effect on everolimus than sirolimus pharmacokinetics and our patients may need a considerably larger dosage of everolimus due to the lack of pharmacokinetic interaction with tacrolimus.

Interestingly, the C/D ratio of everolimus was three times smaller than that of sirolimus in the same patients (**Fig. 3**). Coadministration of inhibitors or inducers of CYP3A or P-glycoprorein would be expected to alter sirolimus or everolimus pharmacokinetics, but comedications in the two patients did not change during the study period. Hepatic impairment would decrease the oral clearance of sirolimus,[15] but neither patient had clinical complications such as hepatic dysfunction. Actually, the trough concentrations of tacrolimus, also metabolized by CYP3A and transported via P-glycoprotein, remained in a similar range during the conversion from sirolimus to everolimus in these patients. Therefore, we consider that a larger dosage is needed for everolimus than sirolimus to maintain the same trough blood concentration in the same patients with tacrolimus. As discussed in the previous paragraph, in the case of concomitant administration of cyclosporine, dosage of everolimus might not be so different from that of sirolimus, because of the more profound pharmacokinetic interaction of cyclosporine with everolimus compared to sirolimus. Pharmacokinetic differences between sirolimus and everolimus with cyclosporine in the same patient should be clarified in future study.

Everolimus has been reported to have a large inter-individual variability in the pharmacokinetics,[16] as also found in our cases. In the time course study, the trough concentrations of everolimus in patients 1 and 2 were similar and peak concentrations and AUC_{0-8} in patient 2 were approximately twice those in patient 1 at dosage of 7 mg and 4.5 mg, respectively (**Fig. 4**). Apparent clearance of everolimus approximately estimated by the dose-normalized AUC_{0-8} seems similar in these patients. In contrast, dose-normalized trough concentrations for everolimus and sirolimus were different as also shown in **Figure 3**. One possible reason for these findings is that the patients had different absorption profiles. In general, the recommended therapeutic range for everolimus is reported as a trough concentration of 3 to 8 ng/mL[17] and the clinical significance of AUC monitoring for everolimus remains to be elucidated.

FPIA is easy and convenient to determine whole blood concentrations of everolimus, but it is known to overestimate everolimus concentrations due to cross-reactivity of the antibody with metabolites of everolimus.[18] Actually, the everolimus concentration measured by FPIA was greater than that obtained by LC/MS over the study period (**Fig. 1**). This finding is consistent with a report using samples from renal transplant recipients.[19] In a recent report,[20] FPIA gave a positive bias of 1.2 ng/mL compared with HPLC-UV. The antibody for everolimus may cross-react with sirolimus because of the similarity in chemical structure between everolimus and sirolimus. Immediately after switching of the mTOR inhibitors, it was considered that few metabolites of everolimus were present in blood, but the values obtained were greater

with FPIA than LC/MS (**Fig. 1**). We consider the difference between the two methods to be caused by cross-reactivity with sirolimus and clarified the cross-reactivity of sirolimus with the antibody used in FPIA for everolimus (**Fig. 2**), as consistent with recent reports.[19,20] However, since the values measured by FPIA exceeded the sum of everolimus and sirolimus concentrations measured by LC/MS immediately after the conversion (**Fig. 1**), we consider that metabolites of sirolimus may also cross-react with the antibody of FPIA. These results indicate that the values of everolimus by the FPIA method should be carefully evaluated especially when transplant patients are switched from sirolimus to everolimus.

In conclusion, we report two cases of changing mTOR inhibitors from sirolimus to everolimus with tacrolimus after pancreatic islet transplantation. Each patient needed a considerably larger dosage of everolimus compared to sirolimus to maintain the same trough blood concentrations, which may be explained by lack of pharmacokinetic interaction between tacrolimus and mTOR inhibitors. The concentrations of everolimus measured by FPIA were considerably greater than those by LC/MS. These findings should provide useful information regarding the replacement of sirolimus with everolimus in transplant patients.

References

1) Shapiro, A. M., Lakey, J. R., Ryan, E. A., Korbutt, G. S., Toth, E., Warnock, G. L., Kneteman, N. M. and Rajotte, R. V.: Islet transplantation in seven patients with type 1 diabetes mellitus using a glucocorticoid-free immunosuppressive regimen. *N. Engl. J. Med.*, **343**: 230–238 (2000).
2) Matsumoto, S., Okitsu, T., Iwanaga, Y., Noguchi, H., Nagata, H., Yonekawa, Y., Yamada, Y., Fukuda, K., Tsukiyama, K., Suzuki, H., Kawasaki, Y., Shimodaira, M., Matsuoka, K., Shibata, T., Kasai, Y., Maekawa, T., Shapiro, J. and Tanaka, K.: Insulin independence after living-donor distal pancreatectomy and islet allotransplantation. *Lancet*, **365**: 1642–1644 (2005).
3) Neuhaus, P., Klupp, J. and Langrehr, J. M.: mTOR inhibitors: an overview. *Liver Transpl.*, **7**: 473–484 (2001).
4) Crowe, A., Bruelisauer, A., Duerr, L., Guntz, P. and Lemaire, M.: Absorption and intestinal metabolism of SDZ-RAD and rapamycin in rats. *Drug Metab. Dispos.*, **7**: 627–632 (1999).
5) Kovarik, J. M., Kalbag, J., Figueiredo, J., Rouilly, M., Frazier, O. L. and Rordorf, C.: Differential influence of two cyclosporine formulations on everolimus pharmacokinetics: a clinically relevant pharmacokinetic interaction. *J. Clin. Pharmacol.*, **42**: 95–99 (2002).
6) Zimmerman, J. J., Harper, D., Getsy, J. and Jusko, W. J.: Pharmacokinetic interactions between sirolimus and microemulsion cyclosporine when orally administered jointly and 4 hours apart in healthy volunteers. *J. Clin. Pharmacol.*, **43**: 1168–1176 (2003).
7) Jacobsen, W., Serkova, N., Hausen, B., Morris, R. E., Benet, L. Z. and Christians, U.: Comparison of the in vitro metabolism of the macrolide immunosuppressants sirolimus and RAD. *Transplant. Proc.*, **33**: 514–515 (2001).
8) Crowe, A. and Lemaire, M.: In vitro and in situ absorption of SDZ-RAD using a human intestinal cell line (Caco-2) and a single pass perfusion model in rats: comparison with rapamycin. *Pharm. Res.*, **15**: 1666–1672 (1998).
9) Hebert, M. F.: Contributions of hepatic and intestinal metabolism and P-glycoprotein to cyclosporine and tacrolimus oral drug delivery. *Adv. Drug Deliv. Rev.*, **27**: 201–214 (1997).
10) Sato, E., Shimomura, M., Masuda, S., Yano, I., Katsura, T., Matsumoto, S., Okitsu, T., Iwanaga, Y., Noguchi, H., Nagata, H., Yonekawa, Y. and Inui, K.: Temporal decline in sirolimus elimination immediately after pancreatic islet transplantation. *Drug Metab. Pharmacokinet.*, **21**: 492–500 (2006).
11) Kovarik, J. M., Kaplan, B., Silva, H. T., Kahan, B. D., Dantal, J., McMahon, L., Berthier, S., Hsu, C. H. and Rordorf, C.: Pharmacokinetics of an everolimus-cyclosporine immunosuppressive regimen over the first 6 months after kidney transplantation. *Am. J. Transplant.*, **3**: 606–613 (2003).
12) Kovarik, J. M., Dantal, J., Civati, G., Rizzo, G., Rouilly, M., Bettoni-Ristic, O. and Rordorf, C.: Influence of delayed initiation of cyclosporine on everolimus pharmacokinetics in de novo renal transplant patients. *Am. J. Transplant.*, **3**: 1576–1580 (2003).
13) Kovarik, J. M., Curtis, J. J., Hricik, D. E., Pescovitz, M. D., Scantlebury, V. and Vasquez, A.: Differential pharmacokinetic interaction of tacrolimus and cyclosporine on everolimus. *Transplant. Proc.*, **38**: 3456–3458 (2006).
14) Wu, F. L., Tsai, M. K., Chen, R. R., Sun, S. W., Huang, J. D., Hu, R. H., Chen, K. H. and Lee, P. H.: Effects of calcineurin inhibitors on sirolimus pharmacokinetics during staggered administration in renal transplant recipients. *Pharmacotherapy*, **25**: 646–653 (2005).
15) Zimmerman, J. J., Lasseter, K. C., Lim, H. K., Harper, D., Dilzer, S. C., Parker, V. and Matschke, K.: Pharmacokinetics of sirolimus (rapamycin) in subjects with mild to moderate hepatic impairment. *J. Clin. Pharmacol.*, **45**: 1363–1372 (2005).
16) Kovarik, J. M., Kahan, B. D., Kaplan, B., Lorber, M., Winkler, M., Rouilly, M., Gerbeau, C., Cambon, N., Boger, R. and Rordorf, C. on behalf of the Everolimus Phase 2 Study Group.: Longitudinal assessment of everolimus in de novo renal transplant recipients over the first post-transplant year: pharmacokinetics, exposure-response relationships, and influence on cyclosporine. *Clin. Pharmacol. Ther.*, **69**: 48–56 (2001).
17) Mabasa, V. H. and Ensom, M. H.: The role of therapeutic monitoring of everolimus in solid organ transplantation. *Ther. Drug Monit.*, **27**: 666–676 (2005).
18) Strom, T., Haschke, M., Boyd, J., Roberts, M., Arabshahi, L., Marbach, P. and Christians, U.: Crossreactivity of isolated everolimus metabolites with the Innofluor Certican immunoassay for therapeutic drug monitoring of everolimus. *Ther. Drug Monit.*, **29**: 743–749 (2007).
19) Salm, P., Warnholtz, C., Boyd, J., Arabshahi, L., Marbach, P. and Taylor, P. J.: Evaluation of a fluorescent polarization immunoassay for whole blood everolimus determination using samples from renal transplant recipients. *Clin. Biochem.*, **39**: 732–738 (2006).
20) Khoschsorur, G., Fruehwirth, F., Zelzer, S., Stettin, M. and Halwachs-Baumann, G.: Comparison of fluorescent polarization immunoassay (FPIA) versus HPLC to measure everolimus blood concentrations in clinical transplantation. *Clin. Chim. Acta.*, **380**: 217–221 (2007).

Cell Transplantation, Vol. 18, pp. 683–688, 2009
Printed in the USA.

0963-6897/09 $90.00 + .00
E-ISSN 1555-3892
www.cognizantcommunication.com

Neovascularization Induced Around an Artificial Device Implanted in the Abdomen by the Use of Gelatinized Fibroblast Growth Factor 2

Takeshi Yuasa,* Jorge D. Rivas-Carrillo,* Nalú Navarro-Alvarez,* Alejandro Soto-Gutierrez,* Yasuhiro Kubota,* Yasuhiko Tabata,† Teru Okitsu,‡ Hirofumi Noguchi,¶# Shinichi Matsumoto,¶# Shuhei Nakaji,# Noriaki Tanaka,* and Naoya Kobayashi*

*Department of Surgery, Okayama University Graduate School of Medicine and Dentistry, Okayama 700-8558, Japan
†Department of Organ Reconstruction and Biomaterials, Institute for Frontier Medical Sciences, Kyoto University, Kyoto 606-8507, Japan
‡Department of Transplant Surgery, Kyoto University Hospital, Kyoto 606-8507, Japan
§Baylor All Saints Islet Cell Laboratory, Fort Worth, TX, USA
¶Baylor Institution for Immunology Research, Islet Cell Transplantation Laboratory, Baylor Research Institute, Dallas, TX, USA
#Department of Biomedical Engineering, Okayama University of Science, Okayama 700-0005, Japan

The development of a bioartificial pancreas (BAP) with immunoisolating fashion has been gaining attention as a new method for treating diabetes. We have been proceeding with the development of a bag-type BAP that can be easily implanted and that allows for the optional injection or rejection of cells at any time. If fibrosis develops around a BAP device, then the permeability of substances transmitted through a semipermeable membrane will decrease, thereby reducing the reactivity with glucose, so it is necessary for the material of the device to have an excellent histocompatibility. Furthermore, in order to improve the efficacy of BAP treatment, it is important to maintain an environment of ample blood flow around the device. We have created a bag-type device for BAP that is 20 × 20 mm in size and comprises two layers of membranes. We have used an EVAL membrane for the outer membrane of the two layers. The EVAL membrane is a semipermeable membrane with good insulin permeability, which functions as an immunoisolation membrane. The inner membrane consists of PAU-coated HD-PE (nonwoven material processed with polyaminourethan) and it is designed to function as a scaffold for cells. We used Lewis rats to determine whether the effectiveness of fibroblast growth factor 2 (bFGF) can be improved by concomitantly using bFGF with a capacity for blood vessel regeneration as well as bFGF immersed in a sheet of gelatin. We placed the BAP in the abdominal cavity and covered it with the greater omentum. We were able to significantly increase the blood flow and the number of new blood vessels in the tissue surrounding the BAP device by using gelatinized bFGF. There were only a few instances of fibrosis as a biological reaction to the EVAL membrane, and the infiltration of inflammatory cells was mild. There were no adverse effects related to implantation of the device. We confirmed in this study that the use of an implantable BAP device and bFGF allowed for a better blood flow around the BAP device. There were only minor instances of fibrosis and inflammation reaction around the BAP, thus indicating the BAP that we are currently developing to have an excellent histocompatibility.

Key words: Bioartificial pancreas; Neovascularization; Fibroblast growth factor 2

INTRODUCTION

In recent years, the implantation of pancreatic islets as treatment for diabetic patients has been attracting attention worldwide as an effective treatment and it has so far been used at many facilities (15,20,22). The rate of withdrawal of insulin by 1 year after implantation of pancreatic islets is reportedly 44%, and the performance of pancreatic islets implants has been improving over the past several years (12,13,21). Possible reasons include multiple implantations of pancreatic islets in a single patient and improvements in the use of immunosuppressive drugs. However, from a long-term perspective, the state of insulin withdrawal is not always maintained. Due to immune reactions, inflammation reactions, and side effects caused by immunosuppressive drugs in the chronic phase after an implantation, the functionality of an implanted pancreatic islets decrease (9,16,23). Fur-

Received October 31, 2008; final acceptance March 30, 2009.
Address correspondence to Naoya Kobayashi, M.D., Ph.D., Department of Surgery, Okayama University Graduate School of Medicine and Dentistry, 2-5-1 Shikata-cho, Okayama, 700-8558, Japan. Tel: (81) 86-235-7485; Fax: (81) 86-235-7485; E-mail: immortal@md.okayama-u.ac.jp

thermore, the use of immunosuppressive drugs not only has adverse effects on the implanted pancreatic islets but it also decreases the immune function of the patient and increases their susceptibility to infections and carcinogens (3,4). In order to solve these problems, the research and development of an artificial pancreas has been proactively pursued. The types of bioartificial pancreas (BAP) that have been reported thus far include an artificial blood vessel type, a microcapsule type, and a macrocapsule type (2,6–8,14,17,18,24). The BAP that we have been seeking to develop may be classified as a macrocapsule type.

One advantage of our BAP is that the use of semipermeable membranes maintains glucose, insulin, and oxygen permeability while also maintaining an immunoisolation state, because cells, antibodies, and complements related to immune reactions cannot permeate the semipermeable membranes. Therefore, it is not necessary to administer any immunosuppressive drugs. In addition, if fibrosis develops around a BAP device after the implantation of the BAP, then the permeability of substances passing through the semipermeable membrane decreases, thereby reducing the reactivity with glucose and further lowering insulin or oxygen permeability. Therefore, the use of a material with a good histocompatibility for the BAP device has made it possible to maintain functionality over long periods without the development of fibrosis around the BAP. In addition, another advantage is that it is equipped with a port for injecting cells to allow for the collecting and refilling of cells when the functionality of the insulin-secreting cells filling the BAP decreases(5,10).

The most important aspect for improving the performance of BAP treatment is the peripheral blood flow environment. We therefore focused on the greater omentum, which has an abundant blood flow. We devised a scheme for maintaining a favorable blood flow environment around the BAP by covering the BAP with the greater omentum. We also looked into increasing the blood flow by concomitantly using basic fibroblast growth factor 2 (bFGF) with blood vessel regeneration capacity (1,19). Because the bFGF has a short half-life, we also examined whether the effectiveness of bFGF can be improved by using bFGF immersed in a sheet of gelatin to add sustained release.

MATERIALS AND METHODS

Method of Constructing a BAP Device

We created a bag-type device for BAP that is 20 × 20 mm in size and comprises two layers of membranes. We used an EVAL membrane for the outer membrane of the two layers. The EVAL membrane is a semipermeable membrane with good insulin permeability and it functions as an immunoisolation membrane. The inner membrane consists of PAU-coated HD-PE (nonwoven material processed with polyaminourethan) and is designed to function as a scaffold for cells. We also attached a port to this bag-type device for injecting cells in order to fill it with cells.

Treatment of the BAP Device With bFGF

After immersing 20 × 20-mm sheets of gelatin with bFGF (50 μg), the sheets were placed on both surface sides of the BAP device (Fig. 1).

Animal Experiments

We used Lewis rats for this study. Under ether anesthesia, we made a small incision that was approximately 20 mm in size in the middle of the rats' abdomen and opened the abdominal cavity. We then placed the BAP device in the abdominal cavity and covered it with the greater omentum (Fig. 2A). After closing the abdominal rectus muscle using sutures, we guided and secured a port for injecting cells subcutaneously and then closed the skin by sewing it up (Fig. 2B, C). We performed the following two experimental groups: group 1: BAP independent (without bFGF) implant group and group 2: bFGF-covered BAP implant rat group. Body weight of the rats was 280.5 ± 1.9 g (mean ± SD) in group 1 and 269.0 ± 3.6 g in group 2.

Measurement of Blood Flow in the Tissue Surrounding the BAP Device

For both groups, we opened the abdomen 2 weeks after the implantation of the BAP devices and measured the blood flow in the tissues using a laser doppler tissue blood flow imager (Advance, Tokyo, Japan) and quantification was determined using Laser FlowGraphy (LFG-1 version 1.0, Softcare).

Histological Examination

For both groups, 2 weeks after implanting the BAP devices, we removed them with the surrounding tissues. These samples were stained with hematoxylin and eosin (H&E) and Elastica van Gieson (EVG) stains to identify the fibrils of elastin in the blood vessels. The number of the induced blood vessels around the BAP device was counted in ten different fields of view.

Statistical Analyses

Mean values are presented with SDs. A Student's *t*-test was used to calculate the significance of difference in mean values. A value of $p < 0.05$ was considered statistically significant.

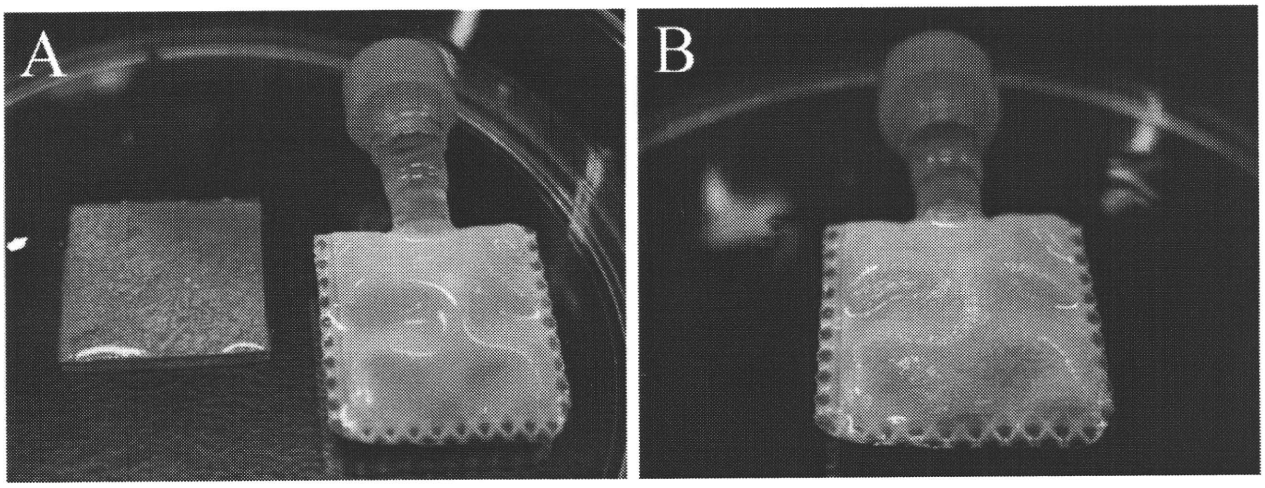

Figure 1. Preparation of gelatinized bFGF for applying the BAP device. (A) Gelatin sheets of 20 × 20-mm in size were immersed with bFGF (50 μg). (B) The sheets were placed on both surface sides of the BAP device.

RESULTS

Use of bFGF Increased Blood Flow in the Tissue Surrounding the BAP Device

Two weeks after implanting the BAP devices, we removed them with the surrounding tissues. We measured the skin blood flow and the blood flow in the BAP implant sites by using a laser blood-flow meter, and we calculated the ratio of BAP site/skin blood flow. Group 1 was 72.6 ± 1.7%, while group 2 was 89.4 ± 3.4% (Fig. 3A). The use of bFGF increased blood flow at the BAP implant site.

bFGF Treatment Increased the Number of New Blood Vessels Around the BAP Device

After formalin fixation of the extracted BAP and the surrounding tissue, we dyed them with EVG to identify the blood vessel fibrils of elastin, and we observed them at a magnification of ?40 to measure the number of blood vessels per field of view. Group 1 was 41.5 ± 3.0, while group 2 was 52 ± 4.28, thus indicating an increase in the number of blood vessels around the BAP (Fig. 3B).

The Biocompatibility of the EVAL Membrane Was Excellent

In both group 1 and group 2, there were no instances of fibrosis as a biological reaction to the EVAL membrane of the BAP surface, and the infiltration of inflammatory cells was not observed at all. The sheets of gelatin were completely absorbed by the body and disappeared (Fig. 4). There were also no adverse effects, such as the formation of abscesses or skin necrosis, in either group. These findings indicated that biocompatibility of the BAP device was excellent.

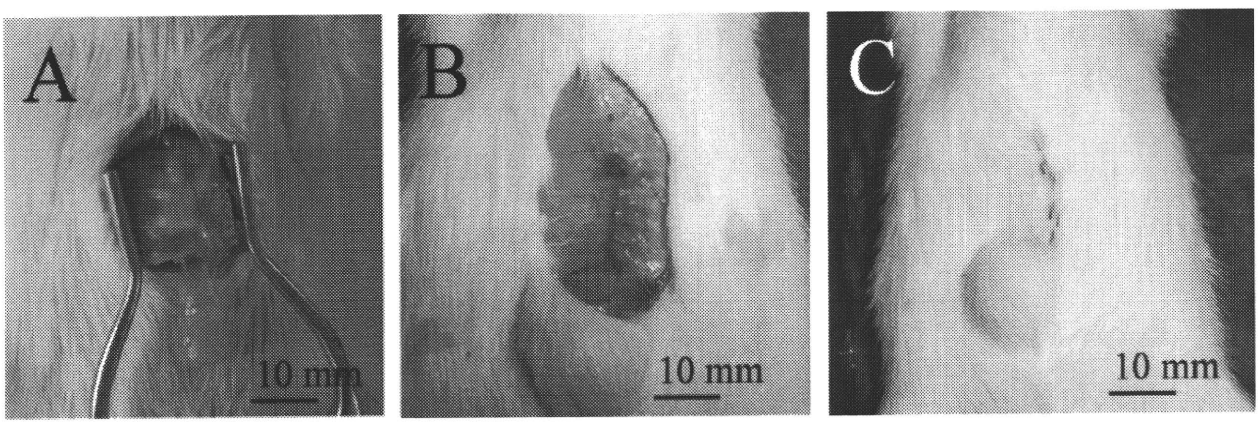

Figure 2. Procedure of an implantation of the BAP device. (A) The BAP device was implanted in the abdominal cavity and covered with the greater omentum. (B) After closing the abdominal rectus muscle we guided and secured a cell injection port subcutaneously. (C) The skin was closed.

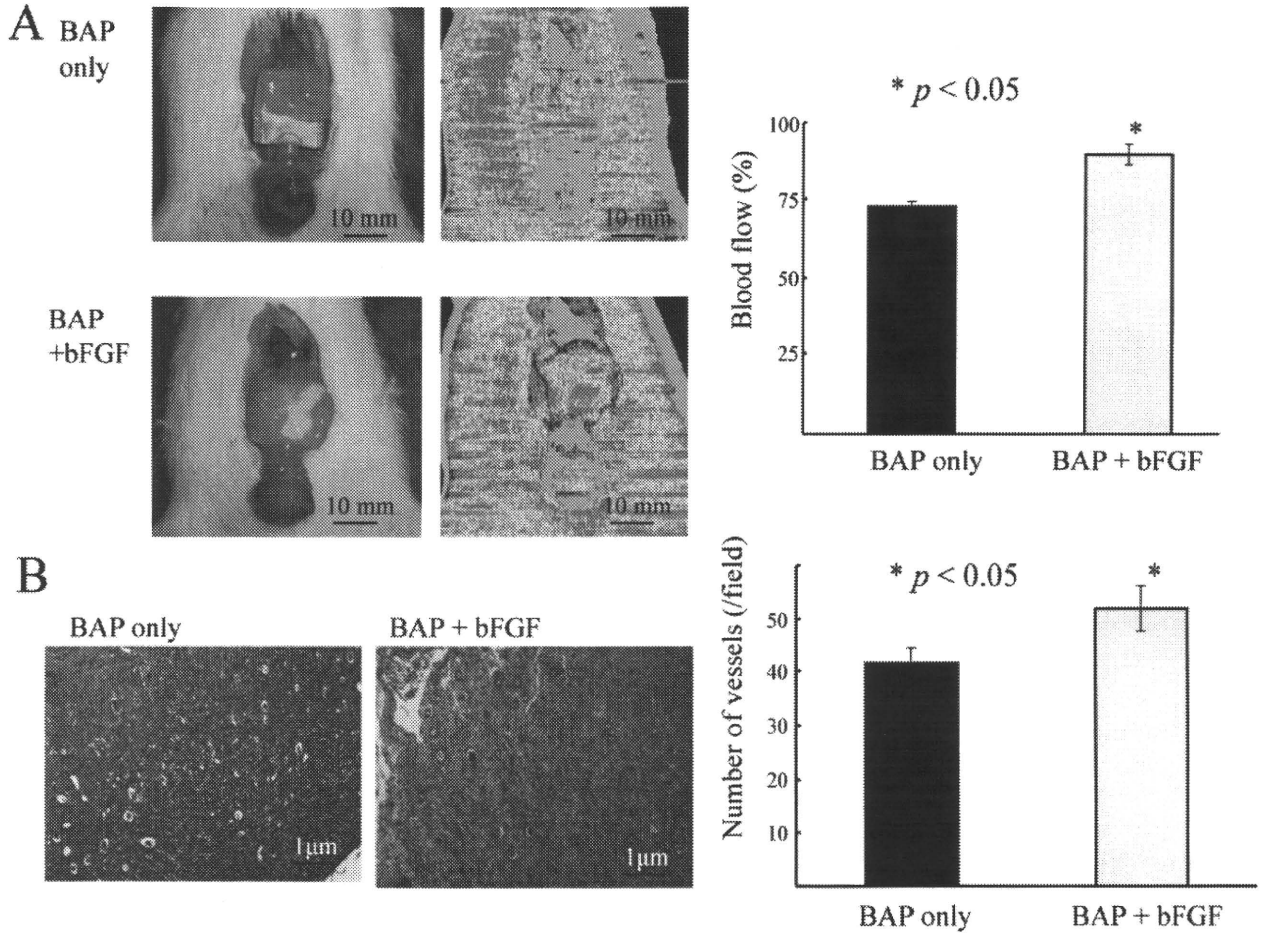

Figure 3. Evaluation of neovascularization around the BAP device. (A) Two weeks after BAP device implantation, we removed them with the surrounding tissues. At the time of removal, we carefully observed the status of vascularization around the devices and then measured blood flow by using a laser blood-flow meter. The ratio of BAP site/skin blood flow was 72.6 ± 1.7% for BAP only (group 1) and 89.4 ± 3.4% for BAP + bFGF (group 2). The use of bFGF significantly increased the blood flow at the BAP implant site. (B) The samples were stained with H&E and EVG stains to identify the blood vessels. The number of the induced blood vessels around the BAP device was counted in 10 different fields of view. bFGF treatment significantly increased the newly induced blood vessels.

DISCUSSION

The measurements of the laser blood-flow meter indicated that the bFGF concomitant use group observed an increase in the blood flow of approximately 20% in comparison to the BAP independent implantation group. In addition, similar results were obtained in the measurements of the number of blood vessels by EVG staining study. We therefore clarified that the use of bFGF enables the blood flow around the BAP device to increase.

Generally, when a foreign object is implanted into a body, inflammation occurs and fibroblasts proliferate around the foreign object. If fibrosis occurs around the BAP device, then insulin-secreting cells in the BAP become damaged, because the ability to modulate blood glucose decreases due to glucose and insulin permeability, and oxygen permeation becomes difficult. There were no instances of fibrosis around the BAP devices, and the inflammation reaction was not observed, thus suggesting that the EVAL membrane that was used as an immunoisolation membrane of the BAP device had a good histocompatibility and that it may be possible to maintain its functionality over a long period after BAP implantation. In the future, we plan to examine the long-term biocompatibility of the BAP device. In addition, because favorable blood vessels were induced around the BAP device at 2 weeks after the implantation, it would be an appropriate time to inject insulin-secreting

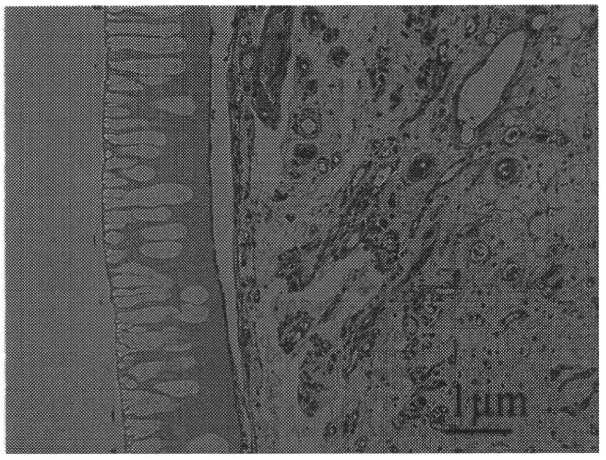

Figure 4. Biocompatibility of the BAP device. In both group 1 and group 2, there were no instances of fibrosis as a biological reaction to the EVAL membrane of the BAP surface, and the infiltration of inflammatory cells was not observed at all. The sheets of gelatin were completely absorbed by the body and disappeared. These findings indicated that biocompatibility of the BAP device was excellent.

cells into the device. The advantage of our BAP device includes an aspect that it is easy to implant and easy to remove. In contrast, the macrocapsule type BAP devices, such as ours, are generally inferior to the microcapsule type ones in terms of oxygen permeability and blood glucose response. In this study, we succeeded in inducing the formation of excellent blood vessels by the use of gelatinized bFGF. Now we plan to first evaluate the performance of syngeneic rat islet transplantation as a source of insulin-secreting cells in our BAP device. Such experiments will provide important clues to create an optimum environment outside and inside the BAP device, while ignoring any immunological reactions. In order to maintain cell function over a long period, it is important to integrate cell matrix biology technologies into the BAP device development (11).

The ultimate aim of this study is to facilitate BAP therapy in diabetic patients using genetically modified artificial cells or xenogenic pancreatic islets or by utilizing its immunoisolation capacity, which is the greatest advantage of BAP. Once when we confirm that xenogenic pancreatic islets can be used as a cell source of BAP, the issue of a shortage of donors, which is one of the most serious issues that we are currently facing in transplantation, can be greatly addressed. Furthermore, when a method of inducing functional differentiated cells from embryonic stem cells or induced pluripotent cells can be developed in the near future, the use of such differentiated insulin-secreting cells will be an attractive source for immunoisolatory BAP, while ignoring the fear of malignant formation of the cells.

REFERENCES

1. Balamurugan, A. N.; Gu, Y.; Tabata, Y.; Miyamoto, M.; Cui, W.; Hori, H.; Satake, A.; Nagata, N.; Wang, W.; Inoue, K. Bioartificial pancreas transplantation at prevascularized intermuscular space: Effect of angiogenesis induction on islet survival. Pancreas 26:279–285; 2003.
2. Gazda, L. S.; Vinerean, H. V.; Laramore, M. A.; Diehl, C. H.; Hall, R. D.; Rubin, A. L.; Smith, B. H. Encapsulation of porcine islets permits extended culture time and insulin independence in spontaneously diabetic BB rats. Cell Transplant. 16:609–620; 2007.
3. Gillard, P.; Ling, Z.; Mathieu, C.; Crenier, L.; Lannoo, M.; Maes, B.; Roep, B.; Gorus, F.; Pipeleers, D.; Keymeulen, B. Comparison of sirolimus alone with sirolimus plus tacrolimus in type 1 diabetic recipients of cultured islet cell grafts. Transplantation 85:256–263; 2008.
4. Hirshberg, B.; Rother, K. I.; Digon, 3rd, B. J.; Lee, J.; Gaglia, J. L.; Hines, K.; Read, E. J.; Chang, R.; Wood, B. J.; Harlan, D. M. Benefits and risks of solitary islet transplantation for type 1 diabetes using steroid-sparing immunosuppression: The National Institutes of Health experience. Diabetes Care 26:3288–3295; 2003.
5. Kobayashi, N. Bioartificial pancreas for the treatment of diabetes. Cell Transplant. 17:11–17; 2008.
6. Kobayashi, T.; Aomatsu, Y.; Iwata, H.; Kin, T.; Kanehiro, H.; Hisanaga, M.; Ko, S.; Nagao, M.; Nakajima, Y. Indefinite islet protection from autoimmune destruction in nonobese diabetic mice by agarose microencapsulation without immunosuppression. Transplantation 75:619–625; 2003.
7. Lacy, P. E.; Hegre, O. D.; Gerasimidi-Vazeou, A.; Gentile, F. T.; Dionne, K. E. Maintenance of normoglycemia in diabetic mice by subcutaneous xenografts of encapsulated islets. Science 254:1782–1784; 1991.
8. Lee, J. I.; Nishimura, R.; Sakai, H.; Sasaki, N.; Kenmochi, T. A newly developed immunoisolated bioartificial pancreas with cell sheet engineering. Cell Transplant. 17:51–59; 2008.
9. Maffi, P.; Bertuzzi, F.; De Taddeo, F.; Magistretti, P.; Nano, R.; Fiorina, P.; Caumo, A.; Pozzi, P.; Socci, C.; Venturini, M.; del Maschio, A.; Secchi, A. Kidney function after islet transplant alone in type 1 diabetes: impact of immunosuppressive therapy on progression of diabetic nephropathy. Diabetes Care 30:1150–1155; 2007.
10. Miki, A.; Rivas-Carrillo, J. D.; Navarro-Alvarez, N.; Soto-Gutierrez, A.; Chen, Y.; Tanaka, K.; Narushima, M.; Tabata, Y.; Okitsu, T.; Noguchi, H.; Matsumoto, S.; Tanaka, N.; Kobayashi, N. Maintenance of neovascularization at the implantation site of an artificial device by bFGF and endothelial cell transplant. Cell Transplant. 15: 893–901; 2006.
11. Navarro-Alvarez, N.; Rivas-Carrillo, J. D.; Soto-Gutierrez, A.; Yuasa, T.; Okitsu, T.; Noguchi, H.; Matsumoto, S.; Takei, J.; Tanaka, N.; Kobayashi, N. Reestablishment of microenvironment is necessary to maintain in vitro and in vivo human islet function. Cell Transplant. 17:111–119; 2008.
12. Noguchi, H.; Matsumoto, S. Islet transplantation at the Diabetes Research Institute Japan. J. Hepatobiliary. Pancreat. Surg. 15:278–283; 2008.

13. Noguchi, H.; Yamada, Y.; Okitsu, T.; Iwanaga, Y.; Nagata, H.; Kobayashi, N.; Hayashi, S.; Matsumoto, S. Secretory unit of islet in transplantation (SUIT) and engrafted islet rate (EIR) indexes are useful for evaluating single islet transplantation. Cell Transplant. 17:121–128; 2008.
14. Omer, A.; Duvivier-Kali, V. F.; Trivedi, N.; Wilmot, K.; Bonner-Weir, S.; Weir, G. C. Survival and maturation of microencapsulated porcine neonatal pancreatic cell clusters transplanted into immunocompetent diabetic mice. Diabetes 52:69–75; 2003.
15. Ricordi, C.; Strom, T. B. Clinical islet transplantation: Advances and immunological challenges. Nat. Rev. Immunol. 4:259–268; 2004.
16. Ryan, E. A.; Lakey, J. R.; Paty, B. W.; Imes, S.; Korbutt, G. S.; Kneteman, N. M.; Bigam, D.; Rajotte, R. V.; Shapiro, A. M. Successful islet transplantation: continued insulin reserve provides long-term glycemic control. Diabetes 51:2148–2157; 2002.
17. Sakata, N.; Gu, Y.; Qi, M.; Yamamoto, C.; Hiura, A.; Sumi, S.; Sunamura, M.; Matsuno, S.; Inoue, K. Effect of rat-to-mouse bioartificial pancreas xenotransplantation on diabetic renal damage and survival. Pancreas 32:249–257; 2006.
18. Sakata, N.; Sumi, S.; Gu, Y.; Qi, M.; Yamamoto, C.; Sunamura, M.; Egawa, S.; Unno, M.; Matsuno, S.; Inoue, K. Hyperglycemia and diabetic renal change in a model of polyvinyl alcohol bioartificial pancreas transplantation. Pancreas 34:458–465; 2007.
19. Sakurai, T.; Satake, A.; Nagata, N.; Gu, Y.; Hiura, A.; Doo-Hoon, K.; Hori, H.; Tabata, Y.; Sumi, S.; Inoue, K. The development of new immunoisolatory devices possessing the ability to induce neovascularization. Cell Transplant. 12:527–535; 2003.
20. Shapiro, A. M.; Lakey, J. R.; Ryan, E. A.; Korbutt, G. S.; Toth, E.; Warnock, G. L.; Kneteman, N. M.; Rajotte, R. V. Islet transplantation in seven patients with type 1 diabetes mellitus using a glucocorticoid-free immunosuppressive regimen. N. Engl. J. Med. 343:230–238; 2000.
21. Shapiro, A. M.; Ricordi, C.; Hering, B. J.; Auchincloss, H.; Lindblad, R.; Robertson, R. P.; Secchi, A.; Brendel, M. D.; Berney, T.; Brennan, D. C.; Cagliero, E.; Alejandro, R.; Ryan, E. A.; DiMercurio, B.; Morel, P.; Polonsky, K. S.; Reems, J. A.; Bretzel, R. G.; Bertuzzi, F.; Froud, T.; Kandaswamy, R.; Sutherland, D. E.; Eisenbarth, G.; Segal, M.; Preiksaitis, J.; Korbutt, G. S.; Barton, F. B.; Viviano, L.; Seyfert-Margolis, V.; Bluestone, J.; Lakey, J. R. International trial of the Edmonton protocol for islet transplantation. N. Engl. J. Med. 355:1318–1330; 2006.
22. Street, C. N.; Lakey, J. R.; Shapiro, A. M.; Imes, S.; Rajotte, R. V.; Ryan, E. A.; Lyon, J. G.; Kin, T.; Avila, J.; Tsujimura, T.; Korbutt, G. S. Islet graft assessment in the Edmonton Protocol: Implications for predicting long-term clinical outcome. Diabetes 53:3107–3114; 2004.
23. Toso, C.; Baertschiger, R.; Morel, P.; Bosco, D.; Armanet, M.; Wojtusciszyn, A.; Badet, L.; Philippe, J.; Becker, C. D.; Hadaya, K.; Majno, P.; Buhler, L.; Berney, T. Sequential kidney/islet transplantation: Efficacy and safety assessment of a steroid-free immunosuppression protocol. Am. J. Transplant. 6:1049–1058; 2006.
24. Weber, L. M.; Cheung, C. Y.; Anseth, K. S. Multifunctional pancreatic islet encapsulation barriers achieved via multilayer PEG hydrogels. Cell Transplant. 16:1049–1057; 2007.

Available online at www.sciencedirect.com
ScienceDirect
Nuclear Medicine and Biology 36 (2009) 869–876
NUCLEAR MEDICINE — AND — BIOLOGY
www.elsevier.com/locate/nucmedbio

Synthesis and evaluation of a radioiodinated lumiracoxib derivative for the imaging of cyclooxygenase-2 expression

Yuji Kuge[a,b,*], Naoyuki Obokata[a], Hiroyuki Kimura[a], Yumiko Katada[a], Takashi Temma[a], Yukihiko Sugimoto[c], Kazuki Aita[a,d], Koh-ichi Seki[d], Nagara Tamaki[e], Hideo Saji[a]

[a]*Department of Patho-Functional Bioanalysis, Graduate School of Pharmaceutical Sciences, Kyoto University, Kyoto 606-8501, Japan*
[b]*Department of Tracer Kinetics and Bioanalysis, Graduate School of Medicine, Hokkaido University, Sapporo 060-8638, Japan*
[c]*Department of Physiological Chemistry, Graduate School of Pharmaceutical Sciences, Kyoto University, Kyoto 606-8501, Japan*
[d]*Central Institute of Isotope Science, Hokkaido University, Sapporo 060-8638, Japan*
[e]*Department of Nuclear Medicine, Graduate School of Medicine, Hokkaido University, Sapporo 060-8638, Japan*

Received 18 February 2009; received in revised form 14 July 2009; accepted 26 July 2009

Abstract

Introduction: Despite extensive attempts to develop cyclooxygenase (COX)-2 imaging radiotracers, no suitable positron emission tomography (PET)/single photon emission computed tomography (SPECT) tracers are currently available for in vivo imaging of COX-2 expression. The aims of this study were to synthesize and evaluate a radioiodinated derivative of lumiracoxib, 2-[(2-fluoro-6-iodophenyl)-amino]-5-methylphenylacetic acid (FIMA), which is structurally distinct from other drugs in the class and has weakly acidic properties, as a SPECT tracer for imaging COX-2 expression.

Methods: The COX inhibitory potency was assessed by measuring COX-catalyzed oxidation with hydrogen peroxide. Cell uptake characteristics of ^{125}I-FIMA were assessed in control and linterfero/interferon-γ-stimulated macrophages. The biodistribution of ^{125}I-FIMA was determined by the ex vivo tissue counting method in rats.

Results: The COX-2 inhibitory potency of FIMA (IC_{50}=2.46 μM) was higher than that of indomethacin (IC_{50}=20.9 μM) and was comparable to lumiracoxib (IC_{50}=0.77 μM) and diclofenac (IC_{50}=0.98 μM). The IC_{50} ratio (COX-1/COX-2=182) indicated FIMA has a high isoform selectivity for COX-2. ^{125}I-FIMA showed a significantly higher accumulation in COX-2 induced macrophages than in control macrophages, which decreased with nonradioactive FIMA in a concentration dependent manner. The biodistribution study showed rapid clearance of ^{125}I-FIMA from the blood and most organs including the liver and kidneys. No significant in vivo deiodination was observed with radioiodinated FIMA.

Conclusions: FIMA showed high inhibitory potency and selectivity for COX-2. Radioiodinated FIMA showed specific accumulation into COX-2 induced macrophages, no significant in vivo deiodination and rapid blood clearance. Radioiodinated FIMA deserves further investigation as a SPECT radiopharmaceutical for imaging COX-2 expression.

Keywords: Cyclooxygenase-2; Inhibitor; Radioiodination; SPECT; Radiopharmaceutical

1. Introduction

Cyclooxygenases (COXs) are the key rate-limiting enzymes in the conversion of arachidonic acid to prostaglandins and thromboxanes. To date, at least two distinct isoforms of the COXs, a constitutive isoform (COX-1) and an inducible isoform (COX-2), and several of their variants have been discovered [1]. COX-2 plays important roles in response to inflammatory stimuli and has been implicated in a number of pathological processes including many human cancers, atherosclerosis and cerebral and cardiac ischemia [2–5]. We have also reported the association of COX-2 expression with cerebral ischemia and

* Corresponding author. Department of Tracer Kinetics and Bioanalysis, Graduate School of Medicine, Hokkaido University, Sapporo 060-8638, Japan. Tel.: +81 11 706 5085, fax: +81 11 706 7155.
E-mail address: kuge@med.hokudai.ac.jp (Y. Kuge).

0969-8051/$ – see front matter © 2009 Elsevier Inc. All rights reserved.
doi:10.1016/j.nucmedbio.2009.07.006

atherosclerosis using rodent and primate models of these diseases [6–11].

Accordingly, noninvasive imaging of COX-2 expression would be useful for early diagnosis and for monitoring the progression and treatment efficacy for such diseases [12,13]. In this regard, several COX-2 inhibitors including ^{18}F-SC58125, ^{18}F-desbromo-DuP-697, ^{11}C-celecoxib, ^{11}C-rofecoxib and ^{123}I-celecoxib analogues have been radiolabeled and evaluated as potential tracers for positron emission tomography (PET) and single photon emission tomography (SPECT) [14–24] (Fig. 1). We have contributed to this area with the synthesis and preliminary evaluation of radioiodinated celecoxib analogues [22]. Results, however, have not been entirely consistent between laboratories due to what is generally ascribed to the relatively high nonspecific binding of these compounds [23–26]. The effect of this high nonspecific binding on results appears to be largely dependent on experimental conditions and could cause inconsistent findings. Thus, no appropriate PET/SPECT tracers are currently available for in vivo imaging of COX-2 expression [23–25]. In the search for suitable PET/SPECT tracers for COX-2 imaging, attempts have recently been made to radiolabel new generation COX-2 inhibitors which have greater inhibitory potencies and selectivities for COX-2 [25–27]. However, to date, the radiolabeled COX-2 inhibitors evaluated as PET/SPECT tracers exclusively possess the same basic skeleton, a cyclic core with two vicinal aryl rings.

Another new generation COX-2 selective inhibitor, lumiracoxib, is structurally distinct from other drugs in the class and has weakly acidic properties [28–31]. The K_i and IC_{50} values of lumiracoxib for COX-2 are better than or comparable to those of other COX-2 inhibitors including celecoxib [28]. Lumiracoxib is distributed and retained in inflamed tissues while being rapidly cleared from plasma with a short elimination half-life [30–32]. Thus, we selected lumiracoxib as a lead compound for a potential COX-2 imaging tracer. In this study, a radioiodinated derivative of lumiracoxib, 2-[(2-Fluoro-6-iodophenyl)-amino]-5-methylphenylacetic acid (FIMA) was synthesized and its potential as an imaging tracer was assessed in both in vitro and in vivo experiments.

2. Materials and methods

2.1. General

Sodium ^{125}I-iodide (642.8 GBq/mg) was purchased from Perkin Elmer Life and Analytical Sciences (Boston, MA, USA). All chemicals used were of reagent grade.

Proton and carbon nuclear magnetic resonance spectra were recorded on a JMM-ECA500KP spectrometer (JEOL, Tokyo, Japan). The chemical shifts are reported in parts per million (ppm) downfield from an internal tetramethylsilane standard. Mass spectra were recorded with a JMS-HX/HX110A, JMS-SX102AQQ or JMS-GC-mate spectrometer (JEOL).

2.2. Synthesis

2.2.1. Synthesis of FIMA (5)

FIMA was synthesized according to the procedure outlined in Fig. 2.

Compound **2** was synthesized in three steps according to the method reported by Acemoglu et al. [33]. Briefly, *p*-iodotoluene (189 μl, 1.4 mmol) was coupled with 2-bromo-6-fluoroaniline (158 μl, 1.4 mmol), utilizing the Pd(0) catalyzed Buchwald–Hartwig reaction, to give 1 as a colorless oil with a yield of 27%. Compound **1** (771.5 mg, 2.75 mmol) was acylated with bromoacetyl bromide (288 μl, 3.30 mmol) and then subjected to a Friedel-Crafts alkylation to obtain **2** as a yellowish powder with a yield of 39% (Mp, 118–120°C).

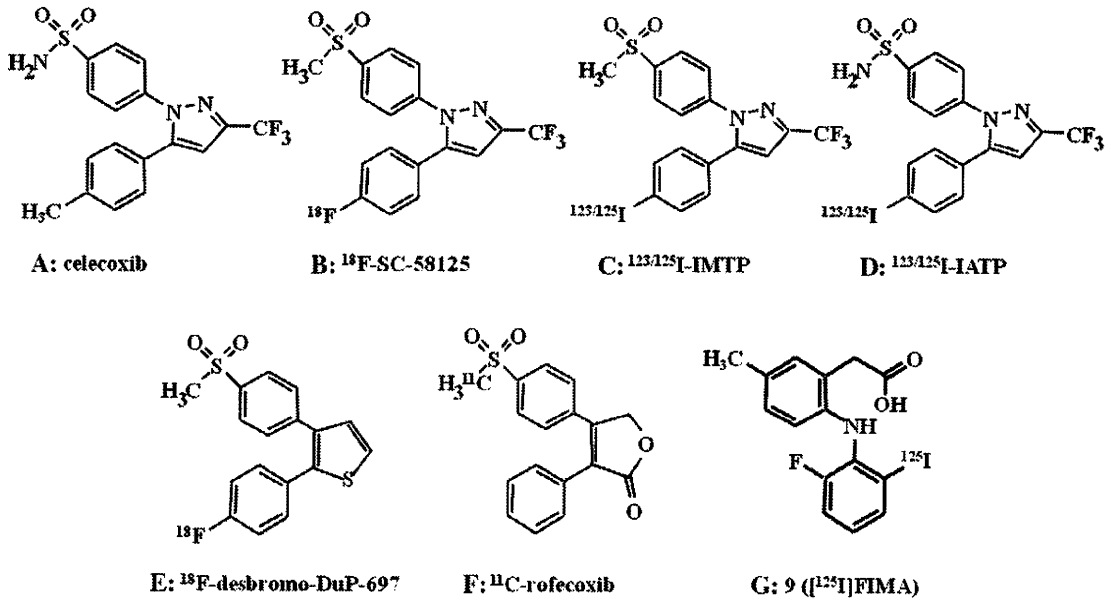

Fig. 1. Chemical structures of radiolabeled COX-2 inhibitors.

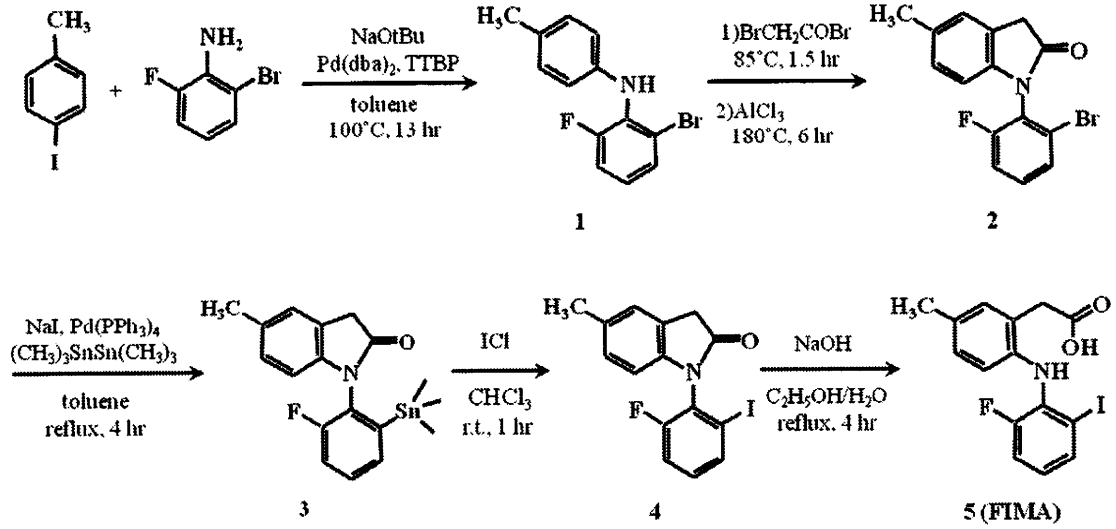

Fig. 2. Synthesis of FIMA (compound 5). Compound **1**, *N*-(2-Bromo-6-fluorophenyl)-4-methylaniline; Compound **2**, *N*-(2′-Bromo-6′-fluorophenyl)-5-methyloxindole; Compound **3**, *N*-(2′-fluoro-6′-trimethylstannanylphenyl)-5-methyl-oxindole; Compound **4**, *N*-(2′-Fluoro-6′-iodophenyl)-5-methyloxindole; Compound **5**, FIMA.

To a solution of **2** (140.7 mg, 0.44 mmol) in 10 ml of toluene at room temperature under a nitrogen atmosphere, NaI (197.6 mg, 1.32 mmol) was added. After stirring at 85°C for 30 min, tetrakis(triphenylphosphine)-palladium(0) (127 mg, 0.11 mmol) and hexamethylditin(IV) (182.3 μl, 0.88 mmol) were added and the solution was refluxed for 4 h. The reaction mixture was filtered and evaporated in vacuo. The residue was purified by silica gel column chromatography (*n*-hexane/ethyl acetate, 6/1) to give **3** as a yellowish powder with a yield of 38% (Mp, 124-127°C).

To a solution of **3** (96.9 mg, 0.24 mmol) in 1 ml of chloroform under an argon atmosphere, iodine monochloride (46.7 mg, 0.29 mmol) in 1 ml of chloroform was added, and the mixture was stirred at room temperature for 1 h. The reaction mixture was washed with saturated sodium thiosulfate and extracted with chloroform. The organic layer was dried over Na_2SO_4, filtered and concentrated in vacuo. The residue was purified by silica gel column chromatography (*n*-hexane/ethyl acetate, 4/1) to give **4** as a pinkish powder with a yield of 85% (Mp, 149-153°C).

To a solution of **4** (61.4 mg, 0.17 mmol) in EtOH/purified water (750 μl/60 μl) under reflux at 95°C, 30% (w/w) NaOH (60 μl) was added dropwise, and the reaction was further refluxed for 4 h. The reaction mixture was allowed to cool to room temperature and then was acidified with 12 N HCl to pH 3.0. Purified water was added to the mixture to give a

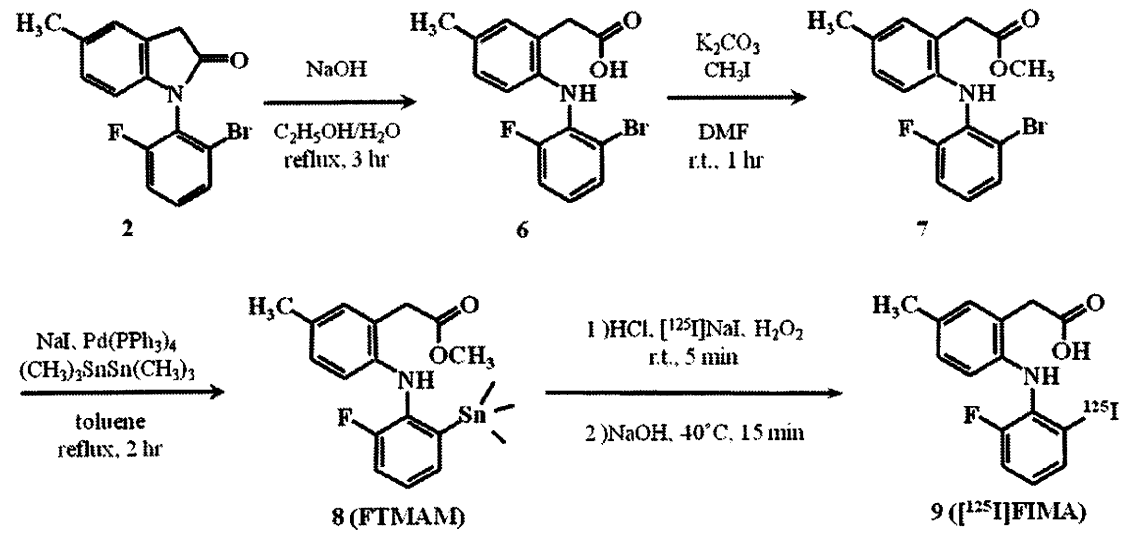

Fig. 3. Synthesis of FTMAM (Compound **8**) and ^{125}I-FIMA (compound **9**). Compound 2, *N*-(2′-Bromo-6′-fluorophenyl)-5-methyloxindole; Compound **6**, 2-[(2-bromo-6-fluorophenyl)amino]-5-methylphenylacetic acid; Compound **7**, 2-[(2-bromo-6-fluorophenyl)amino]-5-methylpheny-lacetic acid methyl ester; Compound **8**, FTMAM; Compound **9**, 2-[(2-fluoro-6-[^{125}I]iodophenyl)amino]-5-methylphenyl-acetic acid (^{125}I-FIMA).

precipitate. The precipitate was filtered, washed with purified water and dried to give **5** as a yellowish ocher powder with a yield of 92% (Mp, 149-152°C). ^{1}H NMR (500 MHz, $CDCl_3$) δ, 7.60 (dt, *J*=8.0, 1.2 Hz, 1H), 7.03-7.07 (m, 2H), 6.96 (dd, *J*=8.0, 1.6 Hz, 1H), 6.74 (td, *J*=8.1, 5.2 Hz, 1H), 6.59 (dd, *J*=8.2, 2.4 Hz, 1H), 6.30 (br s, 1H), 3.79 (s, 2H), 2.28 (s, 3H). HRFABMS: Calcd for $C_{15}H_{13}FINO_2$ $(M+H)^+$, *m/z* 384.9975, found 384.9971.

2.2.2. Synthesis of 2-[(2-fluoro-6-trimethylstannanylphenyl) amino]-5-methylphenylacetic acid methyl ester (8)

2-[(2-Fluoro-6-trimethylstannanylphenyl)amino]-5-methylphenylacetic acid methyl ester (FTMAM) was synthesized according to the procedure outlined in Fig. 3. Compound **6** was synthesized from **2** with a yield of 98% (Mp, 131-134°C) using the same procedure as for FIMA from **4**. To a solution of **6** (142 mg, 0.42 mmol) in 4 ml of Dimethylformamide at room temperature under a nitrogen atmosphere, K_2CO_3 (87.1 mg, 0.63 mmol) was added, and the mixture was stirred for 10 min. Methyl iodide (39.3 μl, 0.63 mmol) was added to the reaction mixture, and the mixture was further stirred at room temperature for 1 h. After the completion of the reaction, ice chilled, purified water was added and the mixture was extracted with ethyl acetate. The organic layer was dried over Na_2SO_4, filtered and concentrated in vacuo. The crude product was purified by silica gel column chromatography (*n*-hexane/ethyl acetate, 4/1) to give **7** as a colorless solid with a yield of 95% (Mp, 55–60°C). FTMAM (**8**) was synthesized from **7** in a similar procedure as for **3** from **2**, except that the crude product was purified by preparative TLC (*n*-hexane/ethyl acetate, 4/1) to give FTMAM (**8**) as a colorless oil with a yield of 30%. Compound **6**: 1H NMR (400 MHz, DMSO-d_6) δ, 7.50 (dt, *J*=8.2, 1.2 Hz, 1H), 7.27 (ddd, *J*=10.9, 8.3, 1.2 Hz, 1H), 7.01-7.07 (m, 3H), 6.90 (dd, *J*=8.0, 1.2 Hz, 1H), 6.39 (dd, *J*=8.0, 2.6 Hz, 1H), 3.63 (s, 2H), 2.21 (s, 3H). HREIMS: Calcd for $C_{15}H_{13}BrFNO_2$ $(M+H)^+$, *m/z* 337.0113, found 337.0120. Compound **7**: 1H NMR (500 MHz, $CDCl_3$) δ, 7.37 (d, *J*=8.2 Hz, 1H), 7.01-7.04 (m, 2H), 6.95 (d, *J*=8.0 Hz, 1H), 6.85 (ddd, *J*=8.2, 8.0, 5.4 Hz, 1H), 6.63-6.65 (m, 2H), 3.76 (s, 2H), 3.74 (s, 3H), 2.28 (s, 3H). HREIMS: Calcd for $C_{16}H_{15}BrFNO_2$ $(M+H)^+$, *m/z* 351.0270, found 351.0264. Compound **8** (FTMAM): ^{1}H NMR (500 MHz, acetone-d_6) δ, 7.32 (dd, *J*=7.2, 1.4 Hz, 1H), 7.25 (ddd, *J*=8.1, 7.2, 4.5 Hz, 1H), 7.17 (ddd, *J*=10.6, 8.1, 1.4 Hz, 1H), 7.02 (s, 1H), 6.86 (d, *J*=8.2 Hz, 1H), 6.59 (br s, 1H), 6.28 (d, *J*=8.2 Hz, 1H), 3.76 (s, 2H), 3.70 (s, 3H), 2.21 (s, 3H), 0.11 (s, 9H). HREIMS: Calcd for $C_{19}H_{24}FNO_2Sn$ $(M+H)^+$, *m/z* 437.0813, found 437.0808.

2.2.3. Synthesis of lumiracoxib

Lumiracoxib, synthesized according to the method of Acemoglu et al. [33] using *p*-iodotoluene and 2-chloro-6-fluoroaniline as starting materials, was obtained as a brownish powder. ^{1}H NMR (400 MHz, DMSO-d6) δ, 12.65 (br s, 1H), 7.35 (dd, *J*=8.3, 1.2 Hz, 1H), 7.23 (ddd, *J*=9.5, 8.3, 1.2 Hz, 1H), 7.06-7.11 (m, 2H), 7.01 (br s, 1H), 6.91 (br d, *J*=8.0 Hz, 1H), 6.42 (dd, *J*=8.3, 2.9 Hz, 1H), 3.65 (s, 2H), 2.21 (s, 3H). HRFABMS: Calcd for $C_{15}H_{13}ClFNO_2$ $(M+H)^+$, *m/z* 293.0619, found 293.0622.

2.3. Radiolabeling

Electrophilic iododestannylation of FTMAM (8) with sodium ^{125}I-iodine and H_2O_2 generated ^{125}I-FIMA as outlined in Fig. 3. Briefly, to a solution of FTMAM in 10 μl of EtOH (1 mg/ml) in a vial, 1 N HCl (15 μl), 12.3 MBq of sodium ^{125}I-iodine in 0.2 N NaOH (7.5 μl, carrier-free) and 30% H_2O_2 (2 μl) were added, and the mixture was stirred at room temperature for 5 min. After cooling with ice, saturated $NaHSO_3$ was added to the reaction mixture to terminate the reaction. The reaction mixture was basified with 1 N NaOH to pH 9.0 at room temperature and then was stirred at 40 °C for 15 min. The solution was applied to a reverse-phase high-performance liquid chromatography (HPLC) column (Cosmosil 5C18-AR-II 4.6 mm injected does × 150 mm, Nacalai Tesque, Kyoto, Japan) and eluted at a flow rate of 1.0 ml/min with 20 mM phosphate buffer (pH 2.5): MeOH=30: 70 for the purification of ^{125}I-FIMA (R_t=17 min). The radiochemical purity of the labeled compound was determined by analytical HPLC using the same conditions as described above. The radiochemical purity and specific activity were determined to be greater than 95% (*n*=3) and 47–72 GBq/μmol (*n*=3), respectively.

2.4. COX inhibitory potency

Peroxidase inhibitory activity of FIMA was assessed by measuring the COX-catalyzed oxidation of *N,N,N′,N′*-tetramethyl-*p*-phenylenediamine (TMPD) by hydrogen peroxide using a commercially available kit (Colorimetric COX Inhibitor Screening Assay Kit, Cayman Chemical, Ann Arbor, MI, USA) as previously described [22]. Briefly, 10 μl of ovine COX-1 or COX-2 solution was added to a 96-well plate with 150 μl of 0.1 mol/L Tris buffer at pH 8.0, 10 μl of heme solution in DMSO, and 10 μl of the test compound (final concentration: 10^{-3}–10^{-9} mol/L). After a 5-min incubation at 25°C, 20 μl of TMPD and 20 μl of 1.1 mM arachidonic acid were added to the mixture. The oxidation of TMPD was monitored by measuring the absorbance of the mixture with a plate reader at 600 nm. Lumiracoxib, diclofenac and indomethacin were used as reference compounds.

2.5. Distribution coefficients

^{125}I-FIMA in a mixture of 2 ml of octanol and 2 ml of 0.1 M phosphate buffer (pH 7.4) was shaken three times for 1 min and then left for 20 min. This procedure was repeated three times, and then the layers were separated by centrifugation. An aliquot of each layer was counted in an auto well gamma counter (Cobra II Auto-Gamma, Packard, Tokyo, Japan). The mean of 3–4 independent octanol-buffer distribution coefficient measurements was expressed as the

$logD_{7.4}$. Radioiodinated analogues of celecoxib, 5-(4-[^{125}I] iodophenyl)-1-[4-(methylsulfonyl)phenyl]-3-trifluoromethyl-1*H*-pyrazole (^{125}I-IMTP) and 5-(4-[^{125}I]iodophenyl)-1-[4-(aminosulfonyl)phenyl]-3-trifluoromethyl-1*H*-pyrazole (^{125}I-IATP) [22] were used as reference compounds.

2.6. In vitro cell uptake study

Since the conventional murine macrophage-like cell line J774.1 is composed of a heterogeneous mixture of cells, JA-4 cells were subcloned from J774.1 cells to obtain a homogeneous cell population. The culturing of JA-4 cells was performed as described previously [34]. In brief, the cells were maintained and cultured in 10 ml of Ham's F-12 medium (Flow Laboratories, McLean, VA, USA), supplemented with 10% heat-inactivated fetal bovine serum (GIBCO, Grand Island, NY, USA), 50 U/ml of penicillin and 50 mg/ml of streptomycin (Flow Laboratories) in a 100-mm plastic dish (Falcon #1001; Becton Dickinson, Lincoln Park, NJ, USA) at 37°C in a CO_2 incubator (5% CO_2-95% humidified air). In order to induce COX-2, aliquots of the cell suspension were placed into 12-well plates and stimulated with linterfero (LPS, 10 μg/ml) and interferon-γ (IFN-γ, 50 U/ml) for 18 h at 37°C in a humidified atmosphere containing 5% CO_2 and 20% O_2. The stimulated and control cells were washed twice with HEPES-buffered Krebs solution (131 mM NaCl, 5.5 mM KCl, 1 mM $MgCl_2$, 2.5 mM $CaCl_2$, 25 mM $NaHCO_3$, 1 mM NaH_2PO_4, 5.5 mM D-glucose, 20 mM HEPES, pH 7.4). After incubation in HEPES buffer at 37°C for 10 min, ^{125}I-FIMA (37 kBq/ml) was added with nonradioactive FIMA (none and 10^{-9} to 10^{-5} M in final concentration), and the cells were incubated at 37°C for 60 min and then were washed twice with ice cold phosphate-buffered saline. The cells were lysed with 1% (w/v) sodium dodecyl sulfate and 10 mM sodium tetraborate decahydrate, collected and counted in an auto well gamma counter (Cobra II Auto-Gamma, Packard, Tokyo, Japan). The protein content was determined using a BCA protein assay kit (Thermo Fisher Scientific, Waltham, MA, USA). The uptake levels of ^{125}I-FIMA are expressed as the percentage of incubated dose per mg protein (% dose/mg protein).

2.7. Western blotting

COX-2 expression levels in the stimulated and control macrophage-like cells (JA-4) were examined by Western blotting. Each cell lysate, prepared from the stimulated and control cells, was mixed with a sample buffer (1% sodium dodecyl sulfate, 10% glycerol, 62.5 mM Tris-HCl (pH 6.8), 0.01% bromo phenol blue, 5% 2-mercaptoethanol) and was subjected to electrophoresis on sodium dodecyl sulfate, 5–20% polyacrylamide gel, followed by transfer to a polyvinylidene difluoride membrane. After blocking with Blocking One (03953-95, Nacalai Tesque, Kyoto, Japan), membranes were incubated with the anti-COX-2 antibody (rabbit polyclonal antibody to murine COX-2 amino acids 570-598, Cayman Chemical), followed by horseradish peroxidase-conjugated swine anti-rabbit immunoglobulin antibody. Bands were visualized by the ECL plus Western Blotting Detection System (RPN2132, GE Healthcare UK. Buckinghamshire, England) using a Luminocapture instrument (BIO-RAD Laboratories, Hercules, CA). Immunoblotting for β-actin was used as a protein loading control.

2.8. Animal experiments

Animal studies were conducted in accordance with institutional guidelines, and experimental procedures were approved by the Kyoto University Animal Care Committee.

Biodistribution studies of ^{125}I-FIMA were performed in male Sprague–Dawley rats (280–310 g). ^{125}I-FIMA (74 kBq/rat) was administered to rats under chloral hydrate anesthesia by tail vein injection. At 10, 30, 60 and 180 min after administration, rats were sacrificed by exsanguination under chloral hydrate anesthesia. Blood and organs were excised and weighed, and radioactivity was measured with an auto well gamma counter (ARC2000, Aloka, Tokyo, Japan). Radioactivity levels in the tissues are expressed as the percentage of injected dose per organ (% ID) and/or the percentage of injected dose per gram of tissue (% ID/g).

3. Results

3.1. Synthesis and radiolabeling

FIMA, FTMAM and lumiracoxib were obtained with overall yields of 7.2%, 6.4% and 19.4%, respectively, from the corresponding starting materials. The radiosynthesis of ^{125}I-FIMA was achieved with an electrophilic iododestannylation reaction. ^{125}I-FIMA was obtained with no carrier being added following separation from the precursor (FTMAM) using reverse phase HPLC with a radiochemical yield of 36–51% (n=3). The radiochemical purity and specific activity were determined to be greater than 95% (n=3) and 47–72 GBq/μmol (n=3), respectively.

3.2. COX inhibitory potency

FIMA inhibited COX-2 in a concentration dependent manner, while showing no inhibitory potency for COX-1 in concentrations up to 10^{-4} M. Table 1 summarizes the IC_{50} values of the test compounds. The IC_{50} value of FIMA was 2.46 μM for COX-2 and 446 μM for COX-1. The COX-2 inhibitory potency of FIMA was higher than that of indomethacin (IC_{50}=20.9 μM) and was comparable to the potencies of lumiracoxib (IC_{50}=0.77 μM) and diclofenac (IC_{50}=0.98 μM). The IC_{50} ratio (COX-1/COX-2) for FIMA was 182 which is comparable to that of lumiracoxib.

3.3. Distribution coefficients

The distribution coefficient ($logD_{7.4}$) of ^{125}I-FIMA was 1.84±0.01 (n=4) and was less than those of the two radioligands, ^{125}I-IMTP ($logD_{7.4}$=3.09±0.11, n=3) and

Table 1
COX inhibitory potency and selectivity of FIMA and reference compounds

Compounds	IC_{50} (μM)		IC_{50} ratio (COX-1/COX-2)
	COX-1	COX-2	
FIMA	446±317	2.46±0.78	182
Lumiracoxib	164±75	0.77±0.21	214
Diclofenac	0.12±0.08	0.98±0.26	0.12
Indomethacin	0.19±0.13	20.9±10.4	0.009

Mean±S.D. for three to four independent experiments.

^{125}I-IATP ($logD_{7.4}$=2.97±0.01, n=4) which were used as reference compounds.

3.4. In vitro cell uptake study

Cell uptake characteristics of ^{125}I-FIMA were assessed in control and LPS/IFN-γ-stimulated macrophages (Fig. 4). The accumulation level of ^{125}I-FIMA in LPS/IFN-γ-stimulated macrophages was significantly higher than that in control macrophages under conditions without nonradioactive FIMA. The accumulation level of ^{125}I-FIMA in LPS/IFN-γ-stimulated macrophages decreased with the addition of nonradioactive FIMA in a concentration dependent manner, while in control macrophages, the accumulation level was unaffected by added nonradioactive FIMA.

Western blot analysis confirmed a significant COX-2 expression in LPS/IFN-γ-stimulated macrophages while no obvious COX-2 expression was observed in control macrophages (Fig. 4B).

3.5. Biodistribution

The biodistribution of ^{125}I-FIMA in normal rats is shown in Table 2. Radioactivity in the blood decreased rapidly and the level was 0.08±0.02% ID/g at 180 min after tracer administration. At 10 min after the injection, high levels of radioactivity were found in the liver and kidneys but

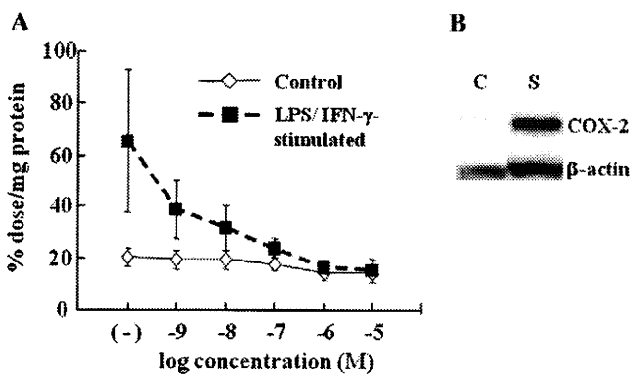

Fig. 4. ^{125}I-FIMA accumulation and COX-2 expression in LPS/IFN-γ-stimulated and control macrophages. (A) ^{125}I-FIMA and nonradioactive FIMA (0, 10^{-9}–10^{-5} M) were incubated with macrophages for 60 min. Mean±S.D. for four experiments. (B) Western blot analysis of COX-2 expression. C, control; S, LPS/IFN-γ-stimulated macrophages.

Table 2
Biodistribution of ^{125}I-FIMA in normal rats

		Time after injection (min)			
		10	30	60	180
Blood	% ID/g	0.55±0.18	0.24±0.02	0.18±0.01	0.08±0.02
Plasma	% ID/g	1.28±0.40	0.57±0.05	0.44±0.05	0.19±0.05
Muscle	% ID/g	0.09±0.03	0.04±0.01	0.03±0.01	0.02±0.00
Heart	% ID/g	0.28±0.10	0.12±0.01	0.08±0.01	0.03±0.01
	% ID	0.24±0.08	0.11±0.01	0.08±0.02	0.03±0.01
Lung	% ID/g	0.36±0.10	0.27±0.19	0.14±0.01	0.07±0.01
	% ID	0.43±0.13	0.38±0.26	0.17±0.02	0.07±0.02
Liver	% ID/g	2.93±1.10	1.04±0.14	0.67±0.05	0.28±0.04
	% ID	25.5±10.4	9.90±0.99	5.88±0.61	2.48±0.35
Kidneys	% ID/g	0.95±0.39	0.81±0.13	0.63±0.09	0.33±0.10
	% ID	2.18±0.87	1.90±0.19	1.49±0.25	0.76±0.23
Pancreas	% ID/g	0.18±0.05	0.10±0.02	0.07±0.01	0.04±0.01
	% ID	0.11±0.06	0.05±0.01	0.03±0.00	0.02±0.01
Spleen	% ID/g	0.14±0.04	0.10±0.05	0.05±0.01	0.03±0.01
	% ID	0.07±0.02	0.05±0.02	0.03±0.00	0.01±0.00
Stomach	% ID/g	0.47±0.19	0.86±0.46	1.28±1.00	0.50±0.27
	% ID	1.00±0.40	1.77±0.97	2.64±1.92	0.95±0.50
Intestine	% ID/g	0.33±0.19	0.46±0.16	0.83±0.14	1.70±0.32
	% ID	4.95±3.08	7.30±3.34	12.16±2.56	22.46±2.39
Brain	% ID/g	0.04±0.02	0.02±0.00	0.02±0.00	0.01±0.00
	% ID	0.08±0.03	0.04±0.00	0.03±0.00	0.01±0.00
Thyroids	% ID/g	1.15±1.06	0.57±0.08	2.28±2.14	6.60±3.58
	% ID	0.01±0.00	0.01±0.00	0.01±0.00	0.03±0.02

Mean±S.D. for five animals.

decreased with time. The radioactivity level in the intestine gradually increased with time and reached 1.70±0.32% ID/g at 180 min. ^{125}I-FIMA showed no significant accumulation in the stomach and thyroid, and the maximum accumulation doses in these tissues were 2.64% ID (60 min) and 0.03% ID (180 min), respectively. Significant levels of radioactivity were not found in the brains of rats.

4. Discussion

In this study, we synthesized a radioiodinated lumiracoxib derivative, 2-[(2-Fluoro-6-[^{125}I]iodophenyl)amino]-5-methylphenyl-acetic acid (^{125}I-FIMA). The potential of radioiodinated FIMA for imaging COX-2 expression was evaluated by in vitro and in vivo experiments. The major findings in this study can be summarized as follows: (1) FIMA had a high inhibitory potency and isoform selectivity for COX-2. (2) ^{125}I-FIMA showed a significantly higher accumulation in COX-2 induced macrophages than in control macrophages, which decreased with the addition of nonradioactive FIMA in a concentration dependent manner. (3) The biodistribution study in normal rats showed rapid clearance of ^{125}I-FIMA from the blood and most organs without significant in vivo deiodination of ^{125}I-FIMA. These results indicate radiolabeled lumiracoxib derivatives have the potential to be PET/SPECT tracers of COX-2 expression. Affinity and specificity including isoform selectivity for COX-2 are indispensable prerequisites of PET/SPECT tracers for imaging the enzyme.

The COX-2 inhibitory potency and isoform selectivity of FIMA were comparable to those of lumiracoxib (Table 1), which suggests that the substitution of chlorine at Position 6 of the 2-phenyl ring (lumiracoxib) with iodine (FIMA) does not greatly affect inhibitory potency or isoform selectivity. The K_i and IC_{50} values of lumiracoxib against COX-2 are reportedly better than or comparable to those of other COX-2 inhibitors including celecoxib [28]. FIMA showed better COX-2 inhibitory potency and isoform selectivity as compared with IMTP, an iodinated methyl sulfone-type analogue of celecoxib (IC_{50} for COX-2=5.16 μM; COX-1/COX-2 IC_{50} ratio>19) [22]. These results motivated us to further evaluate radioiodinated FIMA in in vitro cell uptake and in vivo biodistribution studies.

The in vitro cell uptake study showed that the accumulation level of ^{125}I-FIMA in COX-2 induced macrophages was significantly higher than in control macrophages and decreased with the addition of nonradioactive FIMA in a concentration dependent manner (Fig. 4). These results are indicative of a specific accumulation of ^{125}I-FIMA in COX-2 induced macrophages and are comparable to the recent results with ^{11}C-labeled 1,2-diarylpentens that demonstrated in vitro specificity for COX-2 [27]. In the biodistribution study in normal rats, ^{125}I-FIMA derived radioactivity cleared from all tissues and organs with the exception of the thyroid and intestine within the time period examined (Table 2). Notably, the radioactivity level in the blood was relatively low and showed rapid clearance. In addition, no significant ^{125}I-FIMA accumulation was observed in the stomach and thyroid which indicates that deiodination does not compromise the potentials of the labeled tracer. These results suggest the feasibility of the ^{123}I-labeled compound as a SPECT tracer for COX-2 expression.

Although COX-2 is an inducible isoform, it is found predominantly in the normal brain and kidneys [35]. Consistent with previous studies, a relatively high ^{125}I-FIMA accumulation was observed in the kidneys [14,22]. On the other hand, ^{125}I-FIMA showed little or no accumulation in the brain probably due to its lower lipophilicity ($logD_{7.4}$=1.84) as compared to other COX-2 inhibitors having a cyclic core with two vicinal aryl rings: ^{125}I-IMTP ($logD_{7.4}$=3.09), ^{125}I-IATP ($logD_{7.4}$=2.97 and ^{18}F-desbromo-DuP-697 ($logD_{7.4}$=3.72)[15]. ^{125}I-FIMA may not be a suitable candidate for COX-2 imaging in the brain.

Unfortunately, in the present study, we could not perform experiments to demonstrate in vivo specificity of the candidate compound. We generally perform experiments to block the uptake of a candidate compound in tissues by coinjection with the nonradioactive compound in order to confirm its specific distribution. Such blocking experiments, however, do not appear to be suitable for demonstrating the specific distribution of radiolabeled COX-2 inhibitors because the physiological expression levels of COX-2 are relatively low compared with those in the pathological state. In fact, McCarthy et al. [14] failed to obtain in vivo blocking data to show the specific binding of a radiotracer (^{18}F-SC58125) to COX-2 in rats. As de Vries et al. [24] have pointed out, it is debatable whether the lack of success of labeled COX-2 inhibitors is due to shortcomings of the tracers themselves or inadequate animal models that are used for their evaluation. Thus, it is still unclear whether the unique chemical structure and reduced lipophilicity of lumiracoxib are advantageous for the molecular imaging of COX-2. Experiments in animal models with higher and quantitative expression levels of COX-2 would be necessary to assess the specific binding of tracers to COX-2. Extensive studies to establish adequate animal models applicable to the assessment of COX-2 imaging tracers are greatly needed.

5. Conclusion

In the present study, we synthesized and evaluated the potential of radioiodinated FIMA, a derivative from the new generation COX-2 selective inhibitor, lumiracoxib, which is structurally distinct from other drugs in the class and has weakly acidic properties, as an imaging tracer. The radioiodination of FIMA was successfully achieved. The present results demonstrate FIMA has a high inhibitory potency and isoform selectivity for COX-2. Specific accumulation of ^{125}I-FIMA was observed in COX-2 induced macrophages, which indicates an in vitro specificity to COX-2. In addition, radioiodinated FIMA exhibited rapid blood clearance and no significant in vivo deiodination. These results indicate that radioiodinated FIMA meets the basic requirements for an effective radiotracer and can be a potential candidate as a SPECT tracer for COX-2 expression. Thus, radioiodinated FIMA deserves further investigation as a SPECT radiopharmaceutical for imaging COX-2 expression. Further experiments to demonstrate in vivo specificity of the labeled compound and comparative studies with previous COX-2 imaging tracers are needed.

Acknowledgments

This work was partly supported by a Grant-in-Aid for General Scientific Research from the Japan Society for the Promotion of Science.

References

[1] Davies NM, Good RL, Roupe KA, Yanez JA. Cyclooxygenase-3: axiom, dogma, anomaly, enigma or splice error? Not as easy as 1, 2, 3. J Pharm Sci 2004;7:217–26.

[2] Collaco-Moraes Y, Aspey B, Harrison M, de-Belleroche J. Cyclooxygenase-2 messenger RNA induction in focal cerebral ischemia. J Cereb Blood Flow Metab 1996;16:1366–72.

[3] FitzGerald GA. COX-2 and beyond: approaches to prostaglandin inhibition in human disease. Nat Rev Drug Discov 2003;2:879–90.

[4] Hara K, Kong DL, Sharp FR, Weinstein PR. Effect of selective inhibition of cyclooxygenase 2 on temporary focal cerebral ischemia in rats. Neurosci Lett 1998;256:53–6.

[5] Nogawa S, Zhang F, Ross ME, Iadecola C. Cyclo-oxygenase-2 gene expression in neurons contributes to ischemic brain damage. J Neurosci 1997;17:2746–55.
[6] Yokota C, Inoue H, Kuge Y, Abumiya T, Tagaya M, Hasegawa Y, et al. Cyclooxygenase-2 expression associated with spreading depression in a primate model. J Cereb Blood Flow Metab 2003;23:395–8.
[7] Yokota C, Kaji T, Kuge Y, Inoue H, Tamaki N, Minematsu K. Temporal and topographic profiles of cyclooxygenase-2 expression during 24 h of focal brain ishemia in rats. Neurosci Lett 2004;357: 219–22.
[8] Yokota C, Kuge Y, Inoue H, Tagaya M, Kito G, Susumu T, et al. Post-ischemic cyclooxygenase-2 expression is regulated by the extent of cerebral blood flow reduction in non-human primates. Neurosci Lett 2003;341:37–40.
[9] Yokota C, Kuge Y, Inoue H, Tamaki N, Minematsu K. Bilateral induction of the S-100A9 gene in response to spreading depression is modulated by the cyclooxygenase-2 activity. J Neurol Sci 2005;234: 11–6.
[10] Kaji T, Kuge Y, Yokota C, Tagaya M, Inoue H, Shiga T, et al. Characterisation of [^{123}I]iomazenil distribution in a rat model of focal cerebral ischaemia in relation to histopathological findings. Eur J Nucl Med Mol Imaging 2004;31:64–70.
[11] Kuge Y, Takai N, Ishino S, Temma T, Shiomi M, Saji H. Distribution profiles of membrane type-1 matrix metalloproteinase (MT1-MMP), matrix metalloproteinase-2 (MMP-2) and cyclooxygenase-2 (COX-2) in rabbit atherosclerosis: comparison with plaque instability analysis. Biol Pharm Bull 2007;30:1634–40.
[12] Herschman HR, Talley JJ, DuBois R. Cyclooxygenase 2 (COX-2) as a target for therapy and noninvasive imaging. Mol Imaging Biol 2003;5: 286–303.
[13] de Vries EF. Imaging of cyclooxygenase-2 (COX-2) expression: potential use in diagnosis and drug evaluation. Curr Pharm Des 2006; 12:3847–56.
[14] McCarthy TJ, Sheriff AU, Graneto MJ, Talley JJ, Welch MJ. Radiosynthesis, in vitro validation, and in vivo evaluation of 18F-labeled COX-1 and COX-2 inhibitors. J Nucl Med 2002;43:117–24.
[15] de Vries EF, van Waarde A, Buursma AR, Vaalburg W. Synthesis and in vivo evaluation of 18F-desbromo-DuP-697 as a PET tracer for cyclooxygenase-2 expression. J Nucl Med 2003;44:1700–6.
[16] Wust FR, Hohne A, Metz P. Synthesis of ^{18}F-labelled cyclooxygenase-2 (COX-2) inhibitors via Stille reaction with 4-[^{18}F]fluoroiodobenzene as radiotracers for positron emission tomography (PET). Org Biomol Chem 2005;3:503–7.
[17] Majo VJ, Prabhakaran J, Simpson NR, Van Heertum RL, Mann JJ, Kumar JS. A general method for the synthesis of aryl [^{11}C] methylsulfones: potential PET probes for imaging cyclooxygenase-2 expression. Bioorg Med Chem Lett 2005;15:4268–71.
[18] Prabhakaran J, Majo VJ, Simpson NR, Van Heertum RL, Mann JJ, Kumar JS. Synthesis of [C-11]celecoxib: a potential PET probe for imaging COX-2 expression. J Label Compd Radiopharm 2005;48: 887–95.
[19] Toyokuni T, Kumar JS, Walsh JC, Shapiro A, Talley JJ, Phelps ME, et al. Synthesis of 4-(5-[^{18}F]fluoromethyl-3-phenylisoxazol-4-yl)benzenesulfonamide, a new [^{18}F]fluorinated analogue of valdecoxib, as a potential radiotracer for imaging cyclooxygenase-2 with positron emission tomography. Bioorg Med Chem Lett 2005;15:4699–702.
[20] Yang DJ, Bryant J, Chang JY, Mendez R, Oh CS, Yu DF, et al. Assessment of cyclooxygense-2 expression with ^{99}mTc-labeled celebrex. Anticancer Drugs 2004;15:255–63.
[21] Kabalka GW, Mereddy AR, Schuller HM. Synthesis of an iodine-123-labeled celecoxib analogue: a potential spect agent. J Label Compd Radiopharm 2005;48:295–300.
[22] Kuge Y, Katada Y, Shimonaka S, Temma T, Kimura H, Kiyono Y, et al. Synthesis and evaluation of radioiodinated cyclooxygenase-2 inhibitors as potential SPECT tracers for cyclooxygenase-2 expression. Nucl Med Biol 2006;33:21–7.
[23] Prabhakaran J, Underwood MD, Parsey RV, Arango V, Majo VJ, Simpson NR, et al. Synthesis and in vivo evaluation of [^{18}F]-4-[5-(4-methylphenyl)-3-(trifluoromethyl)-1*H*-pyrazol-1-yl]benzenesul fonamide as a PET imaging probe for COX-2 expression. Bioorg Med Chem 2007;15:1802–7.
[24] de Vries EF, Doorduin J, Dierckx RA, van Waarde A. Evaluation of [(11)C]rofecoxib as PET tracer for cyclooxygenase 2 overexpression in rat models of inflammation. Nucl Med Biol 2008;35:35–42.
[25] Tian H, Lee Z. Synthesis of ^{18}F-labeled cyclooxygenase-2 (COX-2) inhibitor as a potential PET imaging agent. J Label Compd Radiopharm 2006;49:583–93.
[26] Tanaka M, Fujisaki Y, Kawamura K, Ishiwata K, Qinggeletu, Yamamoto F, et al. Radiosynthesis and evaluation of 11C-labeled diaryl-substituted imidazole and indole derivatives for mapping cyclooxygenase-2. Biol Pharm Bull 2006;29:2087–94.
[27] Wuest F, Kniess T, Bergmann R, Pietzsch J. Synthesis and evaluation in vitro and in vivo of a 11C-labeled cyclooxygenase-2 (COX-2) inhibitor. Bioorg Med Chem 2008;16:7662–70.
[28] Esser R, Berry C, Du Z, Dawson J, Fox A, Fujimoto RA, et al. Preclinical pharmacology of lumiracoxib: a novel selective inhibitor of cyclooxygenase-2. Br J Pharmacol 2005;144:538–50.
[29] Stichtenoth DO, Frolich JC. The second generation of COX-2 inhibitors: what advantages do the newest offer? Drugs 2003;63: 33–45.
[30] Buvanendran A, Barkin R. Lumiracoxib. Drugs Today (Barc) 2007;43: 137–47.
[31] Bannwarth B, Berenbaum F. Clinical pharmacology of lumiracoxib, a second-generation cyclooxygenase 2 selective inhibitor. Expert Opin Investig Drugs 2005;14:521–33.
[32] Rordorf CM, Choi L, Marshall P, Mangold JB. Clinical pharmacology of lumiracoxib: a selective cyclo-oxygenase-2 inhibitor. Clin Pharmacokinet 2005;44:1247–66.
[33] Acemoglu M, Allmendinger T, Calienni J, Cercus J, Loiseleur O, Sedelmeier GH, et al. Synthesis of new *N*-aryl oxindoles as intermediates for pharmacologically active compounds. Tetrahedron 2004;60:11571–86.
[34] Katsuyama M, Ikegami R, Karahashi H, Amano F, Sugimoto Y, Ichikawa A. Characterization of the LPS-stimulated expression of EP2 and EP4 prostaglandin E receptors in mouse macrophage-like cell line, J774.1. Biochem Biophys Res Commun 1998;251:727–31.
[35] Kam PC, See AU. Cyclo-oxygenase isoenzymes: physiological and pharmacological role. Anaesthesia 2000;55:442–9.

6394 J. Med. Chem. 2009, 52, 6394–6401
DOI: 10.1021/jm901057p

Journal of Medicinal Chemistry Article

Fluoro-pegylated Chalcones as Positron Emission Tomography Probes for in Vivo Imaging of β-Amyloid Plaques in Alzheimer's Disease

Masahiro Ono,*[,†,‡] Rumi Watanabe,[†] Hidekazu Kawashima,[§] Yan Cheng,[‡] Hiroyuki Kimura,[‡] Hiroyuki Watanabe,[†] Mamoru Haratake,[†] Hideo Saji,[‡] and Morio Nakayama*[,†]

[†]*Department of Hygienic Chemistry, Graduate School of Biomedical Sciences, Nagasaki University, 1-14 Bunkyo-machi, Nagasaki 852-8521, Japan,* [‡]*Department of Patho-Functional Bioanalysis, Graduate School of Pharmaceutical Sciences, Kyoto University, Yoshida Shimoadachi-cho, Sakyo-ku, Kyoto 606-8501, Japan, and* [§]*Department of Nuclear Medicine and Diagnostic Imaging, Graduate School of Medicine, Kyoto University, Shogoin Kawahara-cho, Sakyo-ku, Kyoto 606-8507, Japan*

Received July 16, 2009

This paper describes the synthesis and biological evaluation of fluoro-pegylated (FPEG) chalcones for the imaging of β-amyloid (Aβ) plaques in patients with Alzheimer's disease (AD). FPEG chalcone derivatives were prepared by the aldol condensation reaction. In binding experiments conducted in vitro using Aβ(1−42) aggregates, the FPEG chalcone derivatives having a dimethylamino group showed higher K_i values (20−50 nM) than those having a monomethylamino or a primary amine group. When the biodistribution of ^{11}C-labeled FPEG chalcone derivatives having a dimethyamino group was examined in normal mice, all four derivatives were found to display sufficient uptake for imaging Aβ plaques in the brain. ^{18}F-labeled **7c** also showed good uptake by and clearance from the brain, although a slight difference between the ^{11}C and ^{18}F tracers was observed. When the labeling of Aβ plaques was carried out using brain sections of AD model mice and an AD patient, the FPEG chalcone derivative **7c** intensely labeled Aβ plaques. Taken together, the results suggest **7c** to be a useful candidate PET tracer for detecting Aβ plaques in the brain of patients with AD.

Introduction

The formation of β-amyloid (Aβ[a]) plaques is a key neurodegenerative event in Alzheimer's disease (AD).[1,2] Because the imaging of Aβ plaques in vivo may lead to the presymptomatic diagnosis of AD, many radiotracers that bind to Aβ plaques have been developed.[3,4] Preliminary reports of positron emission tomography (PET) suggested that the uptake and retention of 2-(4′-[^{11}C]methylaminophenyl)-6-hydroxybenzothiazole ([^{11}C]PIB, **1**)[5,6] and 4-*N*-[^{11}C]methylamino-4′-hydroxystilbene ([^{11}C]SB-13, **2**)[7,8] differed between the brain of AD patients and those of controls. However, because ^{11}C is a positron-emitting isotope with a $t_{1/2}$ of just 20 min, efforts are being made to develop comparable agents labeled with the isotope ^{18}F ($t_{1/2}$ = 110 min). [^{18}F]-2-(1-(2-(*N*-(2-fluoroethyl)-*N*-methylamino)-naphthalene-6-yl)ethylidene)malononitrile ([^{18}F]FDDNP, **3**)[9,10] and [^{18}F]-4-(*N*-methylamino)-4′-(2-(2-(2-fluoroethoxy)ethoxy)ethoxy)-stilbene ([^{18}F]BAY94−9172, **4**)[11,12] should be useful as tracers for imaging Aβ plaques in the diagnosis of AD. Recent reports suggest that Aβ aggregates possess multiple ligand-binding sites, the density of which differs.[13−15] Therefore, the development of novel probes that bind Aβ aggregates may lead to critical findings regarding the pathology of AD.

Recently, in a search for novel Aβ-imaging probes, we found that radioiodinated flavone,[16,17] chalcone,[18,19] and aurone[20,21] derivatives, which are categorized as flavonoids, showed excellent characteristics such as high affinity for Aβ aggregates and good uptake into and rapid clearance from the brain. The chalcone structure in particular is considered to be a useful core in the development of new Aβ-imaging probes because it can be formed by a one-pot condensation reaction. In addition, because chalcone derivatives show different characteristics of binding to Aβ aggregates from Congo Red and thioflavin T, they are expected to provide new information from in vivo imaging in AD brains.

In the present study, we designed and synthesized fluorinated chalcone derivatives for the purpose of developing ^{18}F-labeled probes for PET-based imaging of Aβ plaques. The formation of bioconjugates based on pegylation-fluorination resulting in fluoro-pegylated (FPEG) molecules is effective for some core structures of Aβ-imaging probes.[22] We have adopted a novel approach, adding a short PEG (n = 1−3) to the chalcone backbone and capping the end of the ethylene glycol chain with a fluorine atom. Indeed, the most promising ^{18}F-labeled agent **4** possesses PEG (n = 3) in the stilbene backbone. This tracer showed strong affinity (K_i = 6.7 nM) for Aβ plaques, high uptake (7.77%ID/g at 2 min postinjection), and rapid clearance from the mouse brain

*To whom correspondence should be addressed. For M.O.: phone, +81-75-753-4608; fax, +81-75-753-4568; E-mail, ono@pharm.kyoto-u.ac.jp. For M.N.: phone, +81-95-819-2441; fax, +81-95-819-2441; E-mail: morio@nagasaki-u.ac.jp.

[a] Abbreviations: Aβ, β-amyloid; AD, Alzheimer's disease; PET, positron emission tomography; PIB, 2-(4′-methyaminophenyl)-6-hydroxybenzothiazole; SB-13, 4-*N*-methylamino-4′-hydroxystilbene; FDDNP, 2-(1-(2-(*N*-(2-fluoroethyl)-*N*-methylamino)naphthalene-6-yl)ethylidene)-malononitrile; BAY94-9174, 4-(*N*-methylamino)-4′-(2-(2-(2-fluoroethoxy)ethoxy)ethoxy)-stilbene; DMIC, 4-dimethylamino-4′-iodo-chalcone; IMPY, 6-iodo-2-(4′-dimethylamino)phenyl-imidazo[1,2-*a*]pyridine; FPEG, fluoro-pegylated; DAST, diethylamino sulfur trifluoride; DME, 1,2-dimethoxyethane; MEK, methyl ethyl ketone; [^{11}C]methyl triflate, [^{11}C]MeOTf; DAB, 3,3′-diaminobenzidine.

pubs.acs.org/jmc Published on Web 09/16/2009

Scheme 1

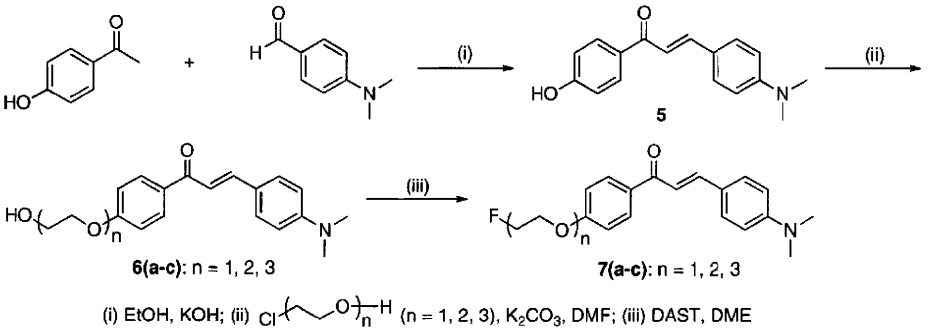

Scheme 2

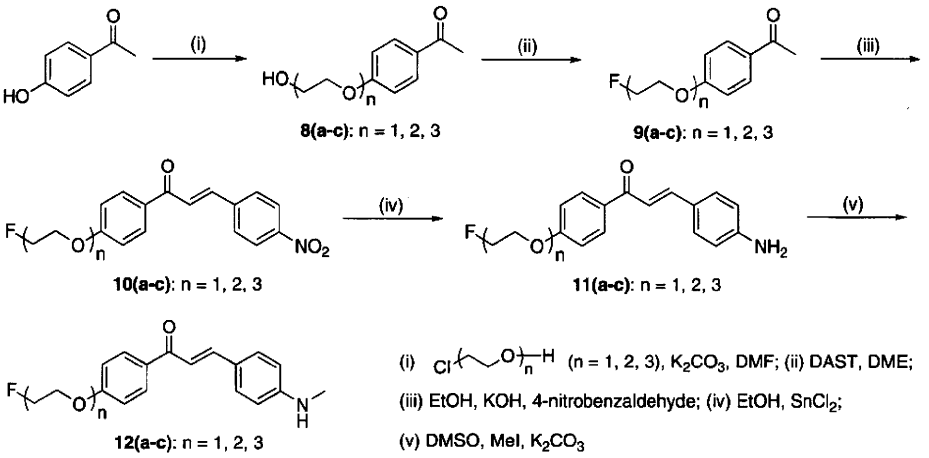

Scheme 3[a]

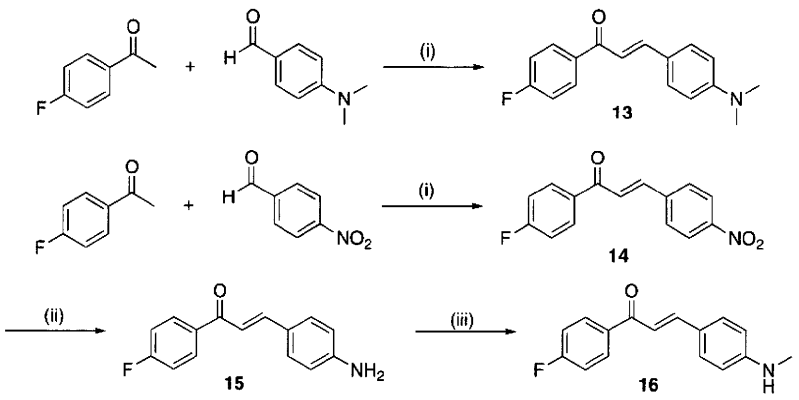

[a](i) EtOH, KOH; (ii) EtOH, $SnCl_2$; (iii) DMSO, MeI, K_2CO_3.

(1.61%ID/g at 60 min postinjection).[12] We adopted the biological data for **4** as criteria to develop novel Aβ-imaging agents. In this study, we synthesized 12 fluorinated chalcones and evaluated their biological potential as Aβ-imaging agents by testing their affinity for Aβ aggregates and Aβ plaques in sections of brain tissue from AD model mice and an AD patient and their uptake by and clearance from the brain in biodistribution experiments using normal mice.

Results and Discussion

The synthesis of the FPEG chalcone derivatives is outlined in Schemes 1, 2, and 3. The most useful way to prepare chalcones is the condensation of acetophenones with ben zaldehydes. Using this process, 4-hydroxyacetophenone or 4-fluoroacetophenone was reacted with 4-dimethylaldehyde to form 4′-hydroxy-4-dimethylamino-chalcone **5** and 4′-fluoro-4-dimethylamino-chalcone **13** in yields of 84.0 and 41.6%, respectively. Compounds **10(a−c)** were synthesized by an aldol reaction between FPEG acetophenone **9(a−c)** and 4-nitrobenzaldehyde. Fluorination of **6(a−c)** and **8(a−c)** to prepare **7(a−c)** and **9(a−c)** was done using diethylamino sulfur trifluoride (DAST) after introducing three oligoethylene glycol molecules into the phenolic OH of **5** and **9(a−c)**. The amino derivatives **11(a−c)** and **15** were readily prepared from **10(a−c)** and **14** by reduction with $SnCl_2$. Conversion of **11(a−c)** and **15** to the monomethylamino derivatives **12(a−c)** and **16** was achieved by methylation with CH_3I under alkaline conditions. Preparation of ^{11}C-labeled compounds was done as in Scheme 4. ^{11}C-labeled chalcones